### Title

Analytical and numerical modeling of RC beam-column joints retrofitted with FRP laminates and hybrid composite connectors




### Authors

Mosallam, Ayman
Allam, Khaled
Salama, Mohamed



### Publication Date

2019-04-01

### DOI

10.1016/j.compstruct.2019.02.032

Peer reviewed

# ANALYTICAL AND NUMERICAL MODELING OF RC BEAM-COLUMN JOINTS RETROFITTED WITH FRP LAMINATES AND HYBRID COMPOSITE CONNECTORS

**Ayman Mosallam[1*], Khaled Allam[2], Mohamed Salama[3]**
[1]University of California, Irvine, Irvine, California, USA
[2]Moffatt & Nichol, Irvine, California, USA
[3]Helwan University, Cairo, Egypt
**Corresponding Author (mosallam@uci.edu)*

## ABSTRACT

This paper summarizes results on an analytical and numerical simulation of structural behavior of reinforced concrete (RC) beam-column joints retrofitted with different types of fiber-reinforced-polymeric (FRP) composite laminates and hybrid connectors. In this study, non-linear numerical simulations for the behavior of reinforced concrete (RC) beam-column joints that were evaluated in another phase of this study. The behavior of a total of eight full-scale interior RC beam-column specimens were numerically evaluated. The interior reinforced concrete (RC) beam-column joint specimens were subjected to both simulated gravity and low-frequency full-cyclic reversal loads. For repair and external strengthening applications, three systems are evaluated including high-strength carbon/epoxy composite laminates, high-modulus carbon/epoxy laminates and E-glass/epoxy external laminates. For bond-slip retrofit, the light-weight hybrid composite connector, developed by the principal author, was evaluated through large-scale tests and is molded numerically. Good correlation between numerical and experimental results is achieved. A comparison between the numerical and experimental results are also presented.

**Keywords:** Beam-column joints; FRP, weak column/strong beam, strengthening, nonlinear analysis, bond slip, shear deficiency, hybrid composite connectors.

## 1. GENERAL

Damage distribution over the height of a building during an earthquake depends on resulting lateral drift distribution. If a building has relatively weak columns, concentration of drifts will likely be at one or few stories and may potentially exceed the columns drift capacity (refer to Figure 1-a). However, if columns are stiff relative to beams, more uniformly drift distribution and less localized damage are likely to occur (refer to Figure 1-b). The majority of buildings that were constructed during 1960's and 1970's did not utilize proper seismic reinforcement detailing of beam-column joints and most in cases, these buildings contained strong beams/weak columns detailing that led to premature failure of the joints (refer to Figure 2). In USA, it is anticipated that there are several thousands of RC frame structures that were designed in accordance to pre-1970 code where no requirements for its resistance to lateral forces making these building vulnerable for even moderate earthquakes (NCEER, 1992).

In order to maintain strong column/weak beam protocol, ACI 318-14 Code (2014) Section 18.7.3.2 requires the following strength check at all beam-to-column connections:

$$\Sigma M_{nc} \geq 6/5 \, \Sigma M_{nb} \tag{1}$$

where: $\Sigma M_{nc}$ is the sum of nominal flexural strength of columns framing into the joint, evaluated at the faces of the joint, and $\Sigma M_{nb}$ is the sum of nominal flexural strengths of the beams framing into the joint, evaluated at the faces of the joint. It should be noted that ACI Code requires that the condition described in Eqn. (1) shall be satisfied for beam moments acting in both directions in the vertical plane of the frame considered.

Based on the observed damages reported from past earthquakes, it was shown that there are two common local joint damages; namely: (i) joint shear local failure, and (ii) bond-slip failure of bottom reinforcement at the joint zone. In past few decades several retrofitting and repair techniques were proposed to upgrade beam-column joint structural performance of old existing RC buildings. In the past, the two popular retrofit and repair techniques employed either steel plating (e.g. Tsonos, 2002) or concrete jacketing (e.g. Karayannis, 2008) and. In late 1990's, fiber-reinforced-polymeric (FRP) composites were introduced to the

construction industry as an alternative technique for repair and rehabilitation of existing structures including RC beam-column joints (Mosallam et al. 2014 and Mosallam, 2008). A comprehensive review on different retrofit and repair techniques for beam column joints is reported by Engindeniz et al. (2005). In 2000, Mosallam an experimental study on cyclic behavior of RC moment frame joints. The tests were conducted on half-scale specimens simulating interior beam-to-column sub-assemblages of a typical RC structure. Two types of composite systems were used including E-glass–epoxy and carbon–epoxy quasi-isotropic laminates. Akguzel and Pampanin (2012) proposed design procedure for the seismic retrofit of RC beam-column joints using FRP composites. A hybrid FRP/steel seismic strengthening of shear deficient beam column joints was proposed by Esmaeeli et al. (2017). Another retrofitting techniques for RC beam-column joints in the form of embedded FRP composite rebars was introduced by Rahman et al. (2018). Santarsiero (2018) presented results of a numerical study that focused on Seismic Behavior of Wide Beam-Column Joints Strengthened with composite laminates. Another study on the use of composites for retrofitting exterior beam-column joints was presented by Roy and Laskar (2018). Recently, Faleschini et al. (2019) presented results of an experimental study on cyclic behavior of RC exterior beam-column joints repaired with externally bonded composites. The damaged specimens were repaired using FRP composite laminates and fiber reinforced cementitious matrix (FRCM) composites. Allam (23010) and Allam et al. (2018) conducted a comprehensive study on evaluating cyclic performance of interior RC beam column joints strengthened with carbon/epoxy and E-glass/epoxy laminates and hybrid composite connectors (HCC). Results of analytical modeling and non-linear numerical simulation of the structural behavior of different beam-column joints retrofitted with different composite systems that were evaluated experimentally by Allam et al. (2018) is presented in this paper.

## 2. ANALYTICAL MODELS FOR RC BEAM-COLUMN JOINTS

In this section, a review of several analytical models that were proposed for simulating behavior of RC beam-column joints are discussed. In addition, analysis and failure criteria for FRP composite retrofitting laminates are also presented in the following sections.

**2.1 Beam-Column Joint Strength Models:** The following are some of the models for analyzing beam –column joints.

*2.1.1 Hwang and Lee Model (1999):* Hwang and Lee (1999) developed a shear strength model for beam-column joint that is commonly known as "Softened Strut-and-Tie" (SST) model. This model satisfies equilibrium, compatibility, and constitutive laws of cracked reinforced concrete. The SST model assumes that the joint shear resisting mechanisms are composed of these three mechanisms; the diagonal strut mechanism, the horizontal mechanism, and the vertical mechanism.

In this model, the iterative solver controls a softening coefficient such that this coefficient satisfies both equilibrium and compatibility, while other parameters, as joint geometry, concrete strength, diagonal strut depth, Young's modulus of reinforcing steel, and horizontal and vertical reinforcement ratios, are given as user input values. The concrete strength in the diagonal strut follows the softening concrete model by Belarbi and Hsu (1995).

*2.1.2 Antonopoulos and Triantafillou Model (2002):* The majority of published analytical models have focused on RC joints without the presence of FRP composites. This model developed formulas for stress and strain at different stages of response for beam-column joint externally reinforced with FRP composites. It is based on Pantazopoulou and Bonacci model (1992) model that was discussed earlier. The free body diagram for typical beam-column joint used to define the forces and stresses on the joint in the horizontal and vertical direction is illustrated in Figure (3).

**2.2 Composite Laminates Stresses and Strains:** For a composite laminate, the matrix formulation of the coupled stress and strain is expressed as:

$$\begin{bmatrix} f_{fh} \\ f_{fv} \\ f_{fhv} \end{bmatrix} = \begin{bmatrix} Q_{11}Q_{12}Q_{13} \\ Q_{12}Q_{22}Q_{23} \\ Q_{13}Q_{23}Q_{33} \end{bmatrix} . \left( \begin{bmatrix} \varepsilon_h \\ \varepsilon_v \\ \gamma \end{bmatrix} - \begin{bmatrix} \varepsilon_{0h} \\ \varepsilon_{0v} \\ \gamma_0 \end{bmatrix} \right) \quad (1)$$

where: $f_{fhv}$ is the shear stress in the FRP composite laminates, $Q_{ij}$ ($i, j$= 1,2,3) is the elements of the FRP material stiffness matrix that depends on the lamina properties, $\varepsilon_h$ is the horizontal strain, $\varepsilon_v$ is the vertical

strain, $\varepsilon_{0h}$ is the initial normal strains in the horizontal direction and $\varepsilon_{0v}$ in the initial normal strains in the vertical direction, $\gamma$ is the shear strain in the joint, and $\gamma_0$ is the initial shear strain at the joint.

The shear strain in the joint is expressed by the following equation:

$$\gamma = \frac{2(\varepsilon_v - \varepsilon_h)}{\tan\theta} = \frac{-2\tan\theta(\varepsilon_v - \varepsilon_h)}{1 - \tan^2\theta} \quad (2)$$

where: $\theta$ is inclination of the maximum principal strain $\varepsilon_1$ from the horizontal axis.

The equilibrium equations are expanded from the matrix formula as follows:

$$\sigma_h = -\rho_{eh} f_h - \rho_f[Q_{11}(\varepsilon_h - \varepsilon_{0h}) + Q_{12}(\varepsilon_v - \varepsilon_{0v}) + Q_{13}(\gamma - \gamma_0)] - \frac{H_h}{bl} \quad (3)$$

$$\sigma_v = -\rho_{ev} f_v - \rho_f[Q_{12}(\varepsilon_h - \varepsilon_{0h}) + Q_{22}(\varepsilon_v - \varepsilon_{0v}) + Q_{23}(\gamma - \gamma_0)] - \frac{V_v}{bd} \quad (4)$$

where $\sigma_h$ and $\sigma_v$ are the horizontal and vertical stress components, respectively, $\rho_{eh}$ and $\rho_{ev}$ are the effective horizontal and vertical reinforcements, respectively, $f_h$ is the average stress in the horizontal steel at centerline of joint width, $f_v$ is the average stress in the column reinforcement at centerline of joint height, $H_h$ is the compressive axial force of the beam, and $V_v$ is the column compressive axial force, *b* is the joint width and *d* is the effective depth of the joint section and *l* is the joint length.

**2.3 Analysis of Joint Shear Deformation:** Reinforced concrete beam-column joint is analyzed following five stages: (i) Stage 1: Prior to yielding of steel reinforcement, (ii) Stage 2: After yielding of horizontal reinforcement and before yielding of vertical reinforcement, (iii) Stage 3: After yielding of both horizontal and vertical reinforcement, (iv) Stage 4: Crushing of concrete, and (v) Stage 5: Failure of FRP. Details of these five stages are described by Antonopoulos and Triantafillou (2002).

**2.4 Steel Rebars Bond-Slip Model:** The analysis for calculating the additional rotation caused by the anchorage slip of the steel reinforcement rebar from the beam-column joints section is based on procedures proposed by Buddha and Ghobarah and (1999) which was built upon previous work reported by Morita and Kaku (1972). This rotation mainly causes inelastic deformation of beam-column joints due to lateral

seismic movement. Figure (4) describes the bilinear *M-θ* relationship due to rebar bond slip. The slip, $\Delta_s$, at the beam-column interface is calculated by integrating the reinforcement rebar strain distribution over the length $L_s$, where $L_s$ is the distance from the beam-column interface to the location where the steel rebar starts to slip (refer to Figure 5).

Prior to yielding ($\varepsilon_s \leq \varepsilon_y$) , the uniform concrete bond stress is expressed as:

$$\begin{aligned} f_b &= 600\varepsilon_s\sqrt{f_c'} \ [MPa] \\ f_b &= 87\varepsilon_s\sqrt{f_c'} \ [ksi] \end{aligned} \tag{5}$$

The equilibrium of a steel rebar segment subjected to a uniform bond stress is:

$$n\pi d_b f_b L_s = n\pi\frac{d_b^2}{4} f_s \tag{6}$$

Therefore:

$$L_s = \frac{d_s f_s}{4 f_b} \tag{7}$$

The stress and strain distribution before yielding of the steel rebar is shown in Figure (5).

From Eqns. (5) and (7), and assuming linear stress-strain relationship of rebar reinforcements, the resultant equation is:

$$L_s = \frac{d_b E_s}{2{,}400\sqrt{f_c'}} \text{, MPa} \qquad [L_s = \frac{d_b E_s}{348\sqrt{f_c'}} \text{, ksi}] \tag{8}$$

$$\Delta_s = \frac{1}{2} L_s \varepsilon_s = \frac{d_b f_s}{4{,}800\sqrt{f_c'}} \text{, MPa} \qquad [\Delta_s = \frac{1}{2} L_s \varepsilon_s = \frac{d_b f_s}{696\sqrt{f_c'}} \text{, ksi}] \tag{9}$$

Prior to yielding ($\varepsilon_s < \varepsilon_y$) , the slope of the bilinear *M-θ* relationship in Figure (4) depends on strain hardening of the longitudinal reinforcement, thickness of the concrete cover relative to the confined cross section of the beam by the transverse reinforcement, amount of transverse reinforcement, size of the yield region, and penetration of yielding into the beam-column joint. The yield development length $L_y$ shown in Figure (5) can be calculated as:

$$L_y = \begin{cases} 2{,}000\alpha - 2{,}000\ mm & for\ 1 < \alpha \leq 1.05 \\ 500\alpha - 425\ mm & for\ \alpha > 1.05 \end{cases}, \alpha = \frac{f_s}{f_y} \leq \frac{f_u}{f_y} \quad (10)$$

where: $f_u$ is the ultimate strength of the reinforcing steel rebar.

Thus:

$$\Delta_s = \left[\frac{L_s + 2L_y}{E_s} + (\alpha - 1)\frac{L_y}{E_{sh}}\right]\frac{f_y}{2} \quad (11)$$

where: $E_{sh}$is the slope of the strain hardening branch of the stress-strain relationship of reinforcement rebar. The upper limits on the length of the slip region $(L_s + L_y)$, i.e. $L_{max} \geq (L_s + L_y)$, and of the yield development length $(L_y)$, i.e. $L_{ymax} \geq L_y$.

*Reinforcement Rebar Yielding before Slippage* ($L_s \leq L_{max}$)*:* The stiffness $K_1$ before yielding in Figure (4) is calculated as:

$$K_1 = \frac{M_y}{\theta_y} = 1200n\pi d_b(d - d')^2 \quad \text{[MPa]} \quad (12)$$

where: $\theta_y = \Delta_y/(d - d')$ and $\Delta_y$ are the rotation and rebar slippage at yielding, respectively, $(d - d')$ is the effective depth of the beam and $d_b$ and $n$ are the rebar diameter and number of the tensile reinforcement rebars in the beam, respectively.

After yielding, stiffness $K_2$ is assumed as a function of $\alpha$ in Eqn. (10). According to Figure (4) and substituting $L_y = L_{ymax}$ and $\alpha = f_{s2}/f_y = M_2/M_y \leq f_u/f_y$ at point 2 with coordinates ($\theta_2$, $M_2$), then:

$$K_2 = \frac{M_2 - M_y}{\theta_2 - \theta_y} = \frac{(\alpha_2 - 1)n\pi\frac{d_b^2}{4}f_y(d - d')^2}{\left[\frac{L_s + 2L_{ymax}}{E_s} + (\alpha_2 - 1)\frac{L_{ymax}}{E_{sh}}\right]\frac{f_y}{2} - \frac{L_s f_y}{2E_s}}$$

$$K_2 = \frac{(\alpha_2 - 1)n\pi d_b^2(d - d')^2 E_s}{2L_{ymax}\left[2 + (\alpha_2 - 1)/\delta\right]} \quad (13)$$

where: $\delta = E_{sh}/E_s$

If $L_s + L_{ymax} > L_{max}$, then $L_y = L_{max} - L_s$ at point 2 (refer to Figure 4), therefore:

$$K_2 = \frac{(\alpha_2 - 1)n\pi d_b^2 (d - d')^2 E_s}{2(L_{max} - L_s)L_{ymax}\left[2 + (\alpha_2 - 1)/\delta\right]} \quad (14)$$

*Reinforcement Rebar Pullout before Yielding* ($L_s > L_{max}$): In this case, steel rebar will pullout prior to yielding and in this case, $K_2$=0. The moment, $M_1$, rotation $\theta_1$, and the corresponding stiffness $K_1$ are calculated as follow:

$$M_1 = n\pi \frac{d_b^2}{4} f_y \left(\frac{L_{\max}}{L_s}\right)(d - d') \quad (15)$$

$$\theta_1 = \frac{\Delta_1}{(d - d')} = \frac{1 f_y L_{max}^2}{2E_s} \frac{1}{L_s} \frac{1}{(d - d')} \quad (16)$$

$$K_1 = \frac{M_1}{\theta_1} = \frac{n\pi d_b^2 E_s (d - d')^2}{2L_{max}} \quad (17)$$

## 3. FINITE ELEMENT (FE) MODELING OF BEAM-COLUMN JOINTS

In this study, non-linear numerical simulations for the behavior of reinforced concrete (RC) beam-column joints that were evaluated by Allam et al. (2018) are presented. The experimental program, a total of eight full-scale interior RC beam-column specimens were evaluated that mimic the interior beam-column joint part between two stories at a reinforced concrete building. The interior reinforced concrete (RC) beam-column joint specimens were subjected to both simulated gravity and low-frequency full-cyclic reversal loads, except for the control specimen (AB-1) that was tested under dynamic impulse loading resembling the near-fault effect during an earthquake event. A typical interior beam-column joint evaluated in Allam et al. (2018) is shown in Figure (6). For repair and external strengthening applications, three systems are evaluated including high-strength carbon/epoxy composite laminates, high-modulus carbon/epoxy laminates and E-glass/epoxy external laminates (see Figure 6). For bond-slip retrofit, the light-weight hybrid composite connector (refer to Figure 10), developed by the principal author, was evaluated through large-scale tests and is molded numerically as it will discussed later in this paper. All external FRP laminates are instrumented with calibrated strain gauges, potentiometers, and linear variable differential transducers (LVDT's) for continuous and accurate

measurements of strain distribution at different critical locations. Table (1) describes the different specimens evaluated by Allam et al. (2018). Details of different fiber architecture for different laminates use in retrofitting and repair different specimens are reported by Allam et al. (2018).

The numerical simulation was performed using ABAQUS (2012) software. The FE models is developed using a concrete damage plasticity model for concrete and Tsai-Wu failure criteria (1971) for predicting the strength of the FRP composites. The results obtained from the finite element analysis are compared with those obtained from experimental data (Allam et al., 2018) for the control specimen as well as for the other different retrofit joint specimens. Figure (7) shows the FE model assembly of concrete and steel rebars reinforcement and the associated mesh.

**3.1 Elements and Material Properties**

*Concrete:* For all joint specimens, concrete is modeled using a solid element with eight nodes with three translation degrees of freedom at each node. The concrete compressive uniaxial stress-strain curve is shown in Figure (8). In the analysis the ABAQUS concrete solid element C3D8R was employed (refer to Figure 9-a). Both elastic and inelastic concrete behavior are incorporated in the FE model. The concrete element is assumed to be homogeneous and an isotropic material. In the analysis, concrete damaged plasticity model (CDP) is used for defining concrete material behavior in the inelastic range (Lee and Fenves, 1998). The main failure mechanisms of the concrete in CDP are (i) the tensile cracking, and (ii) compressive crushing of the concrete. Concrete behavior under axial tension is assumed linear until the formation of the initial cracking at the peak stress known as failure stress. Post failure stress is defined in the ABAQUS in terms of stress versus cracking strain. This behavior allows the effect of interaction between concrete and reinforcement rebar through introducing tension stiffening to the softening side of the curve.

*Steel Rebars Reinforcement:* Steel rebars are modeled using truss elements with two nodes and three translation degrees of freedom at each node. The truss element in ABAQUS model is called T3D2 (refer to Figure 9-b). The longitudinal and transverse steel reinforcement rebar behavior is incorporated in the

FE model as an elastic-plastic material using a bilinear stress strain curve. Slope of the stress-strain curve at the plastic stage is assumed about one-percent of the steel modulus of elasticity. In the analysis, steel rebar elements are connected to the surrounding concrete regions using an embedded element option. This option constrains the translational degrees of freedom of the embedded reinforcement rebar elements nodes defined as a slave element to the degrees of freedom of the surrounding concrete elements nodes defined as a host element.

*Steel Supporting Hinge:* In order to include the exact location of contraflexural point, a triangular steel cube is added as a base support to the bottom of the column (similar to the actual steel hinge in the experimental test). A solid element is used to model the triangular cube and assumed to be linear elastic material. A tie constraint is used to connect bottom of the column to the steel hinge support. The steel hinge solid element used in the FE analysis is shown in Figure (9-c).

*Fiber Reinforcement Polymer (FRP) Composites:* FRP composite laminate is modeled using four nodes shell element S4R (see Figure 9-d). The properties of the unidirectional laminate are incorporated in the model as an orthotropic material. The FRP laminate mechanical properties are defined in the elastic lamina option. A tie constraint is used to connect the lamina shell element to the concrete solid element. The following parameters are entered in the FE model: (i) lamina moduli along and perpendicular to the fibers ($E_{11}$ and $E_{22}$), (ii) lamina shear modulus in the three orthogonal directions ($G_{12}$, $G_{13}$, $G_{23}$), and (iii) lamina Poisson ratio ($v_{12}$) = 0.30.

In ABAQUS, failure criterion for the FRP orthotropic materials is defined in the stress space. The input data for defining the failure criterion is based on the ultimate compressive, tensile and shear strength of the FRP laminate in the two orthogonal directions. The failure index of Tsai and Wu criterion (1971) is used to define the failure criteria in the FE analysis model. The failure criteria in the FE model are based on the following assumptions: (i) full bond between the composite lamina and concrete surface, (ii) lamina's material properties are homogeneous, and (iii) material strength can be experimentally measured from simple tests. Tsai-Wu failure criterion for the two-dimensional stress requires that:

$$I_F = F_1\sigma_{11} + F_2\sigma_{22} + F_{11}\sigma_{11}^2 + F_{22}\sigma_{22}^2 + F_{66}\sigma_{12}^2 + 2F_{12}\sigma_{11}\sigma_{22} < 1.0$$

(18)

where: $I_F$ interaction equation of FRP laminate stresses,$\sigma_{11}, \sigma_{22}, \sigma_{12}$ are the applied longitudinal, transverse and shear stress, respectively. Tsai-Wu failure criteria coefficients are defined as follows:

$$F_1 = \frac{1}{X_t} + \frac{1}{X_c}, F_2 = \frac{1}{Y_t} + \frac{1}{Y_c}, F_{11} = -\frac{1}{X_t X_c}, \; F_{22} = -\frac{1}{Y_t Y_c}, \text{ and } F_{66} = \frac{1}{S^2} \qquad (19)$$

where: $X_t$ is the ultimate tensile strength along the fiber direction, $X_c$ is the ultimate compressive strength along the fiber direction, $Y_t$ is the ultimate tensile strength perpendicular to the fiber direction, $Y_c$ = the ultimate compressive strength perpendicular to the fiber direction, and $S$ is the ultimate shear strength of the fiber. The normalized interaction term according to Tsai-Wu criterion (1971) is expressed as:

$$F_{12} = f^* \sqrt{F_{11}F_{22}}$$

(20)

where: $-1.0 \leq f^* \leq 1.0$ is the range of values of the normalized interaction term for ellipse solution. In this study, the value of discriminant $f^*$ was input in the FE model equal to 0.5, which is commonly used in failure analysis of laminated composites.

*The Hybrid Composite Connectors (HCC):* The hybrid composite connectors (HCC), developed by the principal author, are modeled using a solid element with eight nodes and three translation degrees of freedom at each node. The HCC connector was modeled using the ABAQUS solid element C3D8R (refer to Figure 10). A tie constraint is used to connect the composite connector to the FRP laminate surface. A photograph of the HCC and the solid element used in the FE model analysis is shown in Figure (10).

*Boundary Conditions:* The boundary conditions are set in the model to mimic the experimental test conditions. The bottom of the column is restrained in five degrees of freedom at the $U_x$, $U_y$, $U_z$, $R_x$ and $R_y$

directions. In this scenario, the column is allowed to rotate about $R_z$ only. The pin-pin axial link at the beams' end is assumed in the model as a roller support that released at the $U_x$ and $R_z$. The remaining four boundary conditions $U_y$, $U_z$, $R_x$ and $R_y$ at the beams' end are restrained against movement. The boundary conditions used in the FE modeling is presented in Figure (7-a).

*Loading:* In order to incorporate the gravity and cyclic loads in FE model, two steps are defined in the FE simulation. The gravity load is simulated in the first step as a uniform pressure equal to 2757.91 kPa (0.4 ksi) applied at top of the column. In the experimental program (Allam et al. 2018), a sustained gravity load of 284.69 kN (64.0 kips) was applied during each test which correspond to the applied uniform pressure in the FE model. The lateral cyclic loads are incorporated in the second step of the FE analysis as a monotonic incremental displacement applied tangential to the top surface of the column until failure.

*Finite Element Mesh:* In order to obtain accurate results from the FE model, the size of the element meshing is set to 50.8 mm (2.0″). All model elements are purposely assigned the same mesh size in order to ensure that each two different materials share the same node. The mesh element for concrete, steel rebars, and FRP laminates element are 3D solid, 2D truss and shell, respectively. Figure (7-b) shows the typical mesh for beam-column joint models evaluated in this study.

**3.2 Numerical Results:** In this study, five different cases were conducted to simulate the behavior of different beam-column joint specimens evaluated experimentally by Allam et al. (2018). Load-displacement curve, stresses, and strain were numerically generated for the following cases: (i) as-built specimens, (ii) retrofitted specimen with high-strength carbon/epoxy composite laminates, (iii) retrofitted specimen with E-glass/epoxy composite laminates, (iv) retrofitted specimen with high-modulus carbon/epoxy composite laminates, and (v) retrofitted specimen with both high-strength carbon/epoxy composite laminates and advanced composite connectors.

***3.2.1 Control Specimen:*** In order to validate the experimental test data, the interior RC beam-column joint is modeled and analyzed under both gravity and lateral loads. The gravity load is applied at the first step of analysis followed by lateral incremental displacement load applied tangential at the top face of the upper column in the second step. The boundary conditions at lower column and beam ends are input in the model to mimic the supporting system of the actual specimen (refer to Figure 7-a). The analysis results are presented in the following sections.

*Load-Displacement Curve:* The top of the column load-displacement curve is generated numerically similar to that generated experimentally. Figure (11) shows the FE model load-displacement curve for the control (as-built) specimen. As shown in this figure, the behavior was linear up to a lateral load of 53.4 kN (12.0 kips), after which non-linearity was initiated. In the non-linear portion of the curve, the specimen has reached a maximum lateral load of 70.3 kN (15.8 kips) with an associated lateral displacement of 38.1 mm (1.5″). After reaching the peak point, strength degradation was continued until the end of the numerical run.

*Stresses and Strains:* Stresses and strains are calculated at each step lateral load increments. Numerical results obtained at the last lateral loading step (defined in the analysis as failure) are presented in Figures (12) through (14). The simulated concrete principal stresses and strains at final loading step are presented in Figure (12). As shown, the ultimate compressive stress is located at the bottom left corner of the joint that is accompanied with maximum tensile stress around the center. The concrete principal strain contours shown in Figure (12) indicates that the control specimen maximum and minimum strains are located within the joint region prior to ultimate failure. The ultimate failure is attributed to exceeding the unconfined compressive strain at the beam-column joint the ultimate unconfined concrete compression strain of 0.003 as it was observed in the corresponding test (Allam et al. 2018). The concrete shear stresses, S12, and Von-Mises contours for the as-built beam-column joint specimen are presented in Figure (13). A concrete strut and/or truss are considered to comprise the joint shear resistance mechanism in the joint region. Since the joint shear demand exceeded the resistance capacity of the

concrete strut and truss mechanisms, the joint shear failure was initiated and caused excessive volumetric expansion with the joint area. This is possibility attributed to inadequate confinement provided by horizontal transverse reinforcement that triggered a reduction in joint shear capacity. At a later stage, the FE numerical simulation indicated occurrence of localized damage at the joint region.

The stresses and strain in the reinforcing rebars are shown Figure (14). As shown in this figure, the highest rebar stresses is located at the beam longitudinal steel reinforcement which is attributed to moment induced from horizontal loading at the top of the upper portion of the column.

*State of Damage:* As mentioned earlier, the specimen failure is attributed to shear strength degradation in the joint region. This shear failure is due to a combination of two failure mechanisms; (i) tension cracking and (ii) compression crushing of the concrete at the joint area. Tension damage is resulted from formation of diagonal tension tie inside the joint region, while compression damage is probably caused due to formation of diagonal compression strut as shown in Figure (15). A comparison between simulated and experimental failure of the control specimen is presented in Figure (15)

***3.2.2 Retrofitted Specimen (RS-SC):*** This joint specimen was retrofitted with high-strength carbon/epoxy (CFRP) composite laminates. The lamination schedule of this retrofitted specimen is $[0_2°/+45°/90_2°/-45°/0_2°]_T$. This 8-ply laminates are applied to each face of the joint. Two additional plies are wrapped around the column and beam sections for confinement purpose. The laminates are extended from the joint boundary to a distance of 304.0 mm (12.0″). Each ply of the high-strength CFRP laminate has a thickness equal to 1.0mm (0.04″) with measured ultimate tensile strength of 992.6 MPa (143.9 ksi). In the analysis, a full bond is assumed between the FRP composite laminate and the concrete substrate. The FE results including load-displacement envelope, stresses, strain and Tsai-Wu failure criterion (1971) for FRP composite laminate are presented and discussed in the next section and numerical results are compared with the experimental results.

*Load-Displacement Curve:* In order to validate the experimental data, the load displacement curve is calculated from the FE model. Both the sustained vertical top column load and boundary conditions are

input in the FE analysis model. The load- displacement curve for the retrofitted specimen (RS-SC) is presented in Figure (16). As shown in the figure, the specimen has reached a maximum load of 117.88 kN (26.5 kips) at 114.3 mm (4.5″) lateral displacement that is calculated at the last step (designated herein as failure) during the lateral loading phase. Following this last load increment, the solution diverges due to the rupture of the FRP composite laminates and large deflection.

*Stresses and Strains:* As part of the FE analysis, stresses and strains are computed in the concrete, reinforcing steel rebars, and the FRP composite laminates at each incremental load step. Figure (17) presents the maximum and minimum principal stresses for this specimen. As shown in the figure, most of the damage stress concentrations are located at the top-right and bottom-left of the joint corners due to excessive joint rotation that was the main reason of the FRP debonding at these locations. A similar behavior was observed in the experimental test that was in the form of FRP delamination. Figure (18) shows stress and strain distribution of internal reinforcing steel rebars. As shown, the most stressed locations are at the beam's top-left and bottom-right longitudinal rebars. These simulated results are in good agreement with the experimental results observed during the pull cycle at the ultimate load (Allam et al. 2018). Due to the fact that ABAQUS software does not perform progressive failure analysis, the Tsai-Wu failure criterion (1971) for FRP composite laminates is used. In the strength analysis, the rupture of the FRP laminates is considered the end of the analysis. The Tsai-Wu failure criterion (1971) for the retrofitted specimen (RS-SC) using high-strength CFRP laminates at the joint region and beam-column are presented in Figure (19).

***3.2.3 Retrofitted Specimen (RS-G):*** This joint is retrofitted with ten plies of E-glass/epoxy laminates [$0_3$º/+45º/$90_2$º/-45º/$0_3$º] that were securely bonded on each face of this joint specimen. The unit ply thickness for all composite laminates is 1.14mm (0.045″) with experimentally measured ultimate tensile strength of 625.35 MPa (90.7 ksi). A full bond between concrete and FRP laminates assumption is considered in the model analysis. Numerical results for this specimen are discussed in the following sections.

*Load-Displacement Curve:* As for other joints models described earlier, the load-displacement of this specimen is calculated in the FE model at the same location that was measured in the experimental test. The specimen is subjected to incremental displacement load until failure of the E-glass/epoxy composite laminates. The FE model load-displacement curve is presented in Figure (20). As shown in the figure, the linear portion of the curve ended at of 55.6 kN (12.5 kips), after which nonlinearity was initiated and continued until the solution diverges at an ultimate load of 100.08 kN (22.5 kips).

*Stresses and Strains:* The concrete principal stresses and strain contours for Specimen (RS-G) were simulated numerically at each displacement loading increment. Figure (21) presents the maximum and minimum principal stresses for this specimen. As shown in the figure, the damage is concentrated at the joint's corner that may be attributed to the excessive joint rotation. However, most of high strain concentration is found to populate around the joint center due to stress generated at the compression strut inside the joint region. Figure (22) shows stress and strain distribution in the internal steel reinforcement. In order to evaluate the failure in the laminate, the Tsai-Wu failure criterion (1971) was adopted for the retrofitted specimen (RS-G) as shown in Figure (23).

***3.2.4 Retrofitted Specimen (RS-MC):*** This beam-column specimen was retrofitted with high-modulus carbon/epoxy composites. This specimen (RS-SC) is modeled using dimensions, load pattern, and boundary conditions identical to the other specimens described earlier. The simulated gravity load and lateral forces were applied in two sequential steps similar to the experimental test loading protocol (force-controlled followed by a displacement-control loading protocol). This joint was retrofitted with six plies [0º/+45º/$90_2$º/-45º/0º] of high-modulus CFRP laminates applied at each face of the joint. The unit thickness of each ply is 1.02 mm (0.04″) with an ultimate tensile strength equal to 382.66MPa (51.5 ksi) that was measured experimentally.

*Load-Displacement Curve:* Similar to other specimens, the load-displacement curve was generated to verify the validity of the numerical simulation results with the experimental data. Figure (24) presents the load-displacement curve for the retrofitted specimen (RS-MC) with high-modulus CFRP laminates

As shown in this figure, the behavior of this specimen was linear up to a load level of 44.48 kN (10.0 kips), after which non-linearity was initiated that continued until the failure of the joint specimen. The ultimate simulated load for this specimen was 142.34 kN (32.0 kips) at a column-top lateral displacement of 146.0 mm (5.75″). The load-displacement curve in the non-linear portion shows successive ply failure up to ultimate load before the solution diverges and the analysis was terminated. This rupture of the FRP laminates was attributed to assumption of full bond between the FRP and concrete surface. .

*Stresses and Strains:* As mentioned earlier, model elements stresses and strains were calculated at each loading step increment. Figure (25) presents stress and strain distribution of the joint internal steel reinforcement. Principal stresses and strains are shown in Figure (26). As shown in the figure, the failure occurred due to high stress concentrations zones located at the joint corners and that the highest stress occurred at the longitudinal rebars at the joint zone.

As for previous specimens models, composite laminates failure was simulated using the Tsai-Wu failure criterion (1971) that was applied to laminates at the joint region, as well as those applied to both column and beams locations (see Figure 27).

***3.2.5 Retrofitted Specimen (RS-SCC):*** This specimen simulated a beam-column joint that is deficient both in shear and bond slip capacity and was retrofitted by a combination of CFRP composite laminates (for shear enhancement) and hybrid composite connectors (for bond-slip behavior enhancement). The FE model was subjected to both vertical axial load (simulating the gravity service load) and lateral displacement load (simulating the seismic load) similar to those used in the test. The retrofit scheme of this beam-column joint was in the form of eight-ply laminates [$0_2$º/+45º/$90_2$º/-45º/$0_2$º] made of high-strength CFRP composites that were applied at each face of the joint. Two additional plies were wrapped around the column and beams that were extended to a distance of 304.8 mm (12.0″) from the joint boundaries. Each CFRP ply has a unit thickness of 1.0 mm (0.04″) and an ultimate tensile strength about 992.16 MPa (143.9 ksi). Again, a full bond is assumed between the FRP laminates and the concrete surface. In order to retrofit the discontinuity of the beam bottom longitudinal steel rebars

(bond-slip deficiency), four hybrid composite connectors (HCC) were installed at the four corners of the joint using both high-strength steel bolts and adhesives (refer to Figure 28). A full bond between FRP and connector assumption is considered at the FRP/Connector interface of the four connectors. The FE results including the load displacement envelope, stresses, strain and Tsai-Wu failure criterion (1971) for the FRP composite laminate are presented in the following section.

*Load-Displacement Curve:* The load-displacement curve generated from the numerical simulation was calculated at the same location that was measured in the actual laboratory test. The model is subjected to incremental displacement load until failure of the CFRP laminate and/or the composite connectors. The FE model load-displacement curve for this model is presented in Figure (29). This figure shows that the load-displacement behavior exhibited a linear pattern up to a load level of 80.07 kN (18.0 kips), after which non-linearity is introduced up to the ultimate load. The load continued to increase non-linearly until formation of plastic hinging mechanism at an ultimate load of 169.0 kN (38.0 kips) that corresponds to a lateral displacement of 129.54 mm (5.1″).

*Stresses and Strains:* As stated earlier, both stresses and strain are computed at every increment load or displacement step analogous to the laboratory tests for all joint models simulated in this study. The concrete principal stresses and strains at the last step of the analysis are shown in Figure (30). In this joint model, the majority of the compression stress concentration is located at the edges of the composite connector and away from the column face. This simulated behavior is similar to the concrete crushing observed away from the joint regions during the full-scale laboratory test (Allam et al., 2018). Concrete tension cracks are initiated in the top face of the right beam and the bottom face of the left beam. Figure (31) shows both stress and strain distribution in the internal steel reinforcement. As shown in the figure, the highest stresses in the reinforcement rebars occurred at the plastic hinging location initiated at the edge of the connectors. This behavior was also observed during the full-scale laboratory test indicating good agreement between numerical and experimental results. The Von-Mises stresses of the retrofitted specimen is are presented in Figure (32).

## 4.0 COMPARISON BETWEEN EXPERIMENTAL/FEM RESULTS

In this section, comparisons between the experimental and numerical analysis result are presented. The load-displacement curve of beam-column joint from the finite element models and the envelope of the hysteretic load-displacement response in the push cycles are compared. A summary of load comparison for all specimens evaluated in this study is presented. In addition, analysis for the relationship between the numerical and experimental results are discussed and analyzed.

### 4.1 Load-Displacement Curve

***4.1.1 Control Specimen (AB-2):*** The experimental and numerical load-displacement curves for one of the control specimen experimentally evaluated by Allam et al. (2018) are presented in Figure (34). This figure shows a good agreement between the experimental data and FE model specifically in the linear range. In the non-linear range, the numerical load-displacement curve underestimated the control joint strength by about 10% (97.86kN/22 kips versus 88.96 kN/20.0 kips) as compared to corresponding experimental results. This difference may be attributed several reasons including: (i) the development of severe joint cracks in the actual specimen due to concrete crushing have an effect on the behavior of the actual specimen from the model FE analysis, (ii) the actual supporting system did not perfectly behave the same as the assumed boundary conditions in the FE model, (iii) a full bond assumption with no slippage between the embedded reinforcement rebars was used in the FE model, however, in actuality, there is always some slippage when the rebar elongates under the subjected loads.

***4.1.2 Retrofitted Specimen (RS-SC):*** A comparison between experimental and numerical load-displacement curves is presented in Figure (35). The results from the FE numerical analysis show an overall good satisfactory agreement with the experimental results especially in predicting the ultimate capacity of this joint. In the linear range, the specimen stiffness in the numerical analysis is slightly greater than the actual specimen. The main reason for this difference is due to few assumptions in the

material properties due to insufficient data. Another reason is the presence of micro-crack in the concrete due to shrinkage and temperature change from the day of pouring until the day of testing. In the non-linear range, the ultimate load from the FE model is slightly less than experimental load. The displacement at the ultimate load from the FE model is greater by 75% from the peak load from experimental load. The difference between experimental and numerical displacement value at ultimate load may be attributed to the following reasons: (i) actual behavior of the supporting system in the experimental test and the model boundary conditions, (ii) the assumption of full bond of the embedded reinforcement rebar inside the concrete, however, in the actual specimen, slippage is likely to occur during the elongation of the rebar, (iii) full bond assumption between the composite laminates and the concrete surface is dependent on the quality of surface preparation and applicator skills which may have partially violated, and (iv) for the test specimen, there was delaminating area at the joint corner and rupture of FRP laminate before degradation of the load strength. This has resulted in larger deformation before failure of the beam-column joint.

***4.1.3 Retrofitted Specimen (RS-G):*** Figure (36) presents a comparison between the experimental and numerical load-displacement curves for this specimen retrofitted with E-glass/epoxy laminates. One can see from this figure that there is an overall good agreement throughout the entire range. However, in the linear range, the simulated curve possesses a relatively higher stiffness as compared to the experimental load-displacement curve. The higher stiffness in linear range may be attributed to two reasons: (i) propagation of severe crack in the concrete due to joint core crushing, and (ii) the adoption of the assumption of the full bond between internal steel rebars with no bond slip. Again, the actual specimen would possibly have partial bond-slip during the reinforcement rebar elongation. Also, in the non-linear range, the simulated ultimate load is slightly lower than the corresponding experimental load. The ultimate load in the FE model is the load applied at the last step before the divergence of solution due to excessive cracks that were developed within the joint region that was associated with large deflection. From the figure, one also can notice that the simulated displacement at ultimate load is

higher than the corresponding ultimate load displacement measured from the test. This may be attributed to the adoption of full-bond assumption between GFRP composite laminates and concrete surface. In the actual specimen, delamination at the joint corners and partial debonding inside the joint region before reaching the peak load were observed. This caused additional joint deformation and an increase in joint's lateral displacement.

***4.1.4 Retrofitted Specimen (RS-MC):*** The load-displacement envelope curve generated from the experimental test of the retrofitted specimen (RS-MC) and that obtained from FE model numerical analysis are compared. The experimental and numerically-simulated load-displacement curves for this retrofitted specimen are presented in Figure (37). As shown in the figure, very satisfactory correlation between numerical and experimental stiffness up to a load level of 111.21 kN (25.0 kips). However, the predicted FE ultimate load was higher than the corresponding experimental load by about 22%. As mentioned earlier, the specimen FE model in the numerical analysis is stiffer than the actual specimen in the linear portion. This may be attributed to the fact that the behavior of the actual support system used in the test is not identical to the boundary conditions simulated in the FE model. In the non-linear portion of the load-displacement curve, the experimental ultimate load was lower than the numerically-simulated ultimate load by about 30%. This may be attributed to the excessive deflection in the non-linear range and debonding of the FRP from the concrete surface that was observed at the joint corner. Because of the low strength properties of the high-modulus CFRP composite laminate (as compared to high-strength CFRP), the specimen experienced a severe degradation in the load capacity once the debonding was initiated. This behavior was not captured in the numerical model analysis because of the adoption of the full bond assumption between composites and concrete.

***4.1.5 Retrofitted Specimen (RS-SCC):*** In this section, a comparison between the experimental test data and the FE model analysis results for the retrofitted specimen with high-strength CFRP composite laminates and advanced composite connectors are presented. Figure (38) shows the load-displacement curve for both of the experimental results and the FE model analysis. As mentioned earlier, joint

stiffness generated from numerical simulation is slightly higher than the experimentally-measured stiffness in the linear range. The main reason is the presence of severe cracks in the concrete due to joint crushing. In the non-linear range (refer to Figure 38), the ultimate load generated from the FE model is slightly higher than experimental load. The displacement at the ultimate load from the FE model is lower than the displacement measured from the test by about 8%. This difference may be attributed due to the following reasons: (i) difference between actual behavior of the supporting system used in the experiment and that simulated via typical FE modeling boundary conditions, (ii) the adoption of full-bond assumption between internal reinforcing steel rebars and concrete, and (iii) the use of the assumption that a full bond exists between composite laminates and the concrete in the FE model. However, in the actual specimen, observations violating such assumption was in the form of delamination and debonding of portions of the composite laminates at the joint region corner area.

## 5. EXPERIMENTAL vs. CODE PREDICTED JOINT STRENGTH

A comparison of the joint shear strength between the experimental results and FEMA 356 is presented in Table (1). The shear strength calculated based on the FEMA is underestimating the actual joint shear by about 28%. Also, a shear stress comparison between the experimental results and the ACI-ASCE 352R2-02 for the deficient control specimen (AB-2) is presented in Table (2). The shear stress from the ACI equation is higher than the one obtained from the experimental test by about 31% (Allam et al. 2018).

## 6. SUMMARY

Table (4) shows a summary of the ultimate load at failure for both of the experimental test data and the FE model numerical analysis. The table also presents the ratio between ultimate load from experimental test and numerical FE model. A comparison of the ultimate strength between the experimental and FE numerical analysis is shown in Figure (39).

## REFERENCES

ABAQUS, C. (2012). Analysis User's Manual, Version 6.12, Dassault Systèmes Simulia Corp., Providence, RI, USA.

ACI-ASCE Committee 352 (2002). "Recommendations for Design of Beam-Column Connections in Monolithic Reinforced Concrete Structures," (ACI 352R-02), American Concrete Institute (ACI), Farmington Hills, MI, USA.

Akguzel, U., & Pampanin, S. (2011). "*Assessment and design procedure for the seismic retrofit of reinforced concrete beam-column joints using FRP composite materials*," Journal of Composites for Construction, 16(1), 21-34.

Allam, K. H. (2010). Analytical and experimental evaluation of seismic performance of interior RC beam-column joints strengthened with FRP composites. Ph.D. Thesis, Department of Civil & Environmental Engineering, University of California, Irvine, USA,

Allam, K., Mosallam, A.S., and M.A. Salama (2018). "*Experimental Evaluation of Seismic Performance of Interior RC Beam-Column Joints Strengthened With FRP Composites*," Submitted for Publication, Composites Part B: Engineering.

Antonopoulos, C., and Triantafillou, T. C., (2002), "*Analysis of FRP- Strengthened Beam-Column Joints*," Journal of Composite Construction, 6(1), 41-51.

Belarbi, A., & Hsu, T. T. (1995). "*Constitutive laws of softened concrete in biaxial tension compression*," ACI Structural Journal, 92(5), 562-573.

Beres, A., El-Borgi, S., White, R. N., & Gergely, P. (1992). Experimental results of repaired and retrofitted beam-column joint tests in lightly reinforced concrete frame buildings, NCEER Technical Report, October.

Biddah, A., & Ghobarah, A. (1999). "*Modelling of shear deformation and bond slip in reinforced concrete joints*," Structural Engineering and Mechanics, 7(4), 413-432.

Engindeniz, M., Kahn, L. F., & Abdul-Hamid, Z. (2005). "*Repair and strengthening of reinforced concrete beam-column joints: State of the art*," ACI structural journal, 102(2), 1.

Esmaeeli, E., Danesh, F., Tee, K. F., & Eshghi, S. (2017). "*A combination of GFRP sheets and steel cage for seismic strengthening of shear-deficient corner RC beam-column joints*," Composite Structures, 159, 206-219.

Faleschini, F., Gonzalez-Libreros, J., Zanini, M. A., Hofer, L., Sneed, L., & Pellegrino, C. (2019). "*Repair of severely-damaged RC exterior beam-column joints with FRP and FRCM composites*," Composite Structures, Volume 207, January, pp. 352-363.

FEMA, P. (2000). Commentary for the seismic rehabilitation of buildings. FEMA-356, Federal Emergency Management Agency, Washington, DC., USA.

Karayannis, C.G., Chalioris, C.E., and G. M. Sirkelis (2008). "*Local retrofit of exterior RC beam–column joints using thin RC jackets: an experimental study,"* J. Earthquake Eng. Struct Dyn., 37(5):727–46.

Lee, J., & Fenves, G. L. (1998). "*Plastic-damage model for cyclic loading of concrete structures*," Journal of engineering mechanics, 124(8), 892-900.

Ma, C., Wang, D., & Wang, Z. (2017). "*Seismic retrofitting of full-scale RC interior beam-column-slab subassemblies with CFRP wraps,*" Composite Structures, 159, 397-409.

Morita, S., and Kaku, T. (1972). "*Pullout of the beam bar from beam-column subassemblages,"* Proceedings of Annual Meeting of the Architectural Institute of Japan, AIJ, pp. 1099-1100.

Mosallam, A. S., Bayraktar, A., Elmikawi, M., Pul, S., & Adanur, S. (2014). "*Polymer Composites in Construction: An Overview*," SOJ Mater Sci. Eng. 2 (1), 25. Polymer Composites in Construction: An Overview.

Mosallam, A. S. (2008). *"Structural upgrade of reinforced concrete column-tie beam assembly using FRP composites,"* American Concrete Institute, SP-258, 63-74.

Mosallam AS. (2000). "*Strength and ductility of reinforced concrete moment frame connections strengthened with quasi-isotropic laminates*," Compos. Part B-Eng., 31(6–7):481–97.

Rahman, R., Dirar, S., Jemaa, Y., Theofanous, M., & Elshafie, M. (2018). "*Experimental behavior and design of reinforced concrete exterior beam-column joints strengthened with embedded bars*," ASCE Journal of Composites for Construction.

Roy, B., & Laskar, A. I. (2018). "*Cyclic Performance of Beam-Column Subassemblies with Construction Joint in Column Retrofitted with GFRP*," Structures, June, Vol. 14, pp. 290-300. Elsevier.

Santarsiero, G. (2018). FE Modelling of the Seismic Behavior of Wide Beam-Column Joints Strengthened with CFRP Systems. Buildings, 8(2), 31.

Tsai, S.W., and E.M. Wu (1971). "*A general theory of strength for anisotropic materials*," J. Composite Mat., 5:58-80.

Tsonos AG. (2002). "*Seismic repair of exterior R/C beam-to-column joints using two-sided and three-sided jackets,*" Struct. Eng. Mech., 13(1):17–34.

## LIST OF TABLES

**Table (1):** Description of Different Beam-Column Joints Specimens Evaluated Experimentally by Allam et al. (2018)

| Group | Code | Specimen Description | Loading Pattern |
|---|---|---|---|
| ***Control (As-built)*** | AB-1 | Unconfined Joint according to Pre-1970 code | Dynamic |
| | AB-2 | Unconfined Joint according to Pre-1970 code | Quasi-static |
| | AB-3 | Unconfined Joint & discontinuity of beam bottom rebar according to Pre-1970 code | Quasi-static |
| | AB-3 | Confined Joint according to ACI 318-14 code | Quasi-static |
| ***Repaired*** | AR-2 | Repaired joint with high-strength CFRP laminates | Quasi-static |
| ***Retrofit*** | RS-SC | Strengthened joint with high strength CFRP laminates | Quasi-static |
| | RS-G | Strengthened joint with GFRP laminates | Quasi-static |
| | RS-MC | Strengthened joint with high-modulus CFRP laminates | Quasi-static |
| | RS-SCC | Strengthened joint with high-strength CFRP laminates & advanced composite connectors | Quasi-static |

**Table (2):** A Comparison between Joint Shear Strength and FEMA 356 (2000)

| Specimen ID | $V_{\max}$ ($FEMA$ 356) kN (kips) | $V_{\max}$ ($Experimental$) kN (kips) | $\frac{V_{\max}\ (FEMA\ 356)}{V_{\max}\ (Experimental)}$ |
|---|---|---|---|
| Control Specimen (AB-2) | 513.0 (115.3) | 718.0 (161.5) | 0.72 |
| Control Specimen (AB-4) | 770.0 (173.1) | 821.0 (184.6) | 0.94 |

**Table (3):** A Comparison between Experimental Joint Shear Stress and ACI-ASCE352-02

| | $\tau_{\max}$ $(ACI - ASCE)$ MPa(psi) | $\tau_{\max}$ $(Experimental)$ MPa (psi) | $\frac{\tau_{\max}\ (ACI - ASCE)}{\tau_{\max}\ (Experimental)}$ |
|---|---|---|---|
| Control Specimen (AB- 2) | 9.095 (1,318.7) | 6.963 (1,009.5) | 1.31 |

**Table (4):** Comparison between the Experimental and FE Model Ultimate Load

| | ***Experimental Ultimate Load kN (kips)*** | ***FE Model Ultimate Load kN (kips)*** | $\frac{FE\ Model}{Experimental}$ |
|---|---|---|---|
| Control (AB-2) | 97.5 (21.9) | 89.0 (20.0) | 0.90 |
| Retrofitted (RS-SC) | 130.8 (29.4) | 120.2 (27.0) | 0.92 |
| Retrofitted (RS-G) | 109.9 (24.7) | 130.8 (29.4) | 1.19 |
| Retrofitted (RS-MC) | 108.1 (24.3) | 142.4 (32.0) | 1.31 |
| Retrofitted (RS-SCC) | 151.3 (34.0) | 172.2 (38.7) | 1.13 |

## LIST OF FIGURES

**Figure (37):** Comparison of Load-Displacement Curve for Retrofitted Specimen (RS-MC).
**Figure (38):** Comparison of Load-Displacement Curve for Retrofitted Specimen (RS-SCC).
**Figure (39):** Comparison of Ultimate Load between Experimental and FE Model.

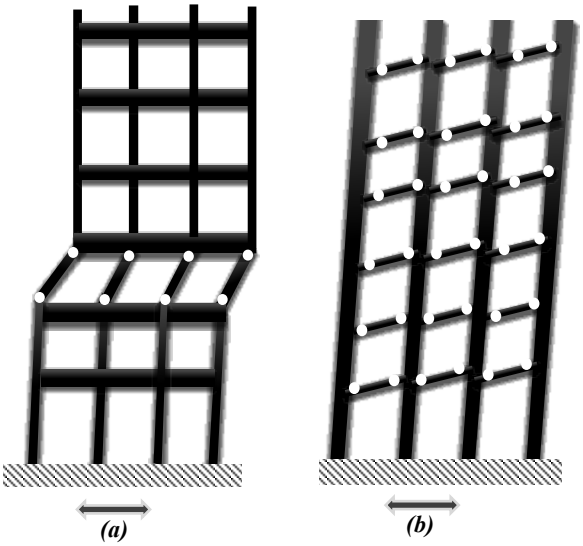


**Figure (1):** Side-sway Mechanisms of Frames: *(a) Strong beam/Weak Column Collapse Mechanism, and (b) Strong Column/Weak Beam Collapse Mechanism.*


**Figure (2):** Weak-Column Strong-Beam Failure (*2005 Kashmir Earthquake*)

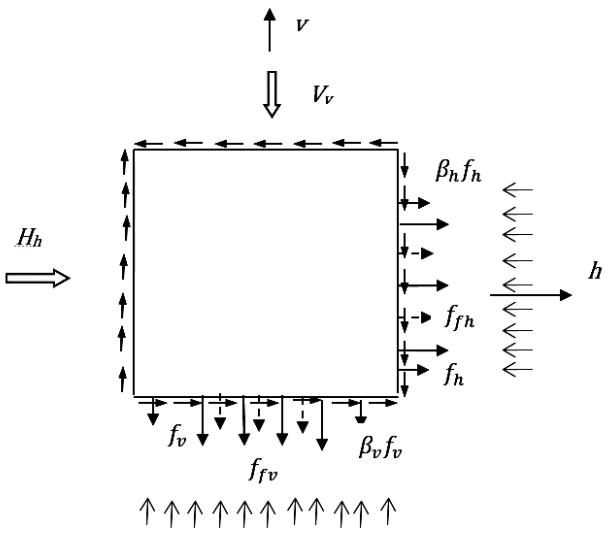


**Figure (3):** Stress Equilibrium of Beam-Column Joint Horizontal and Vertical Forces

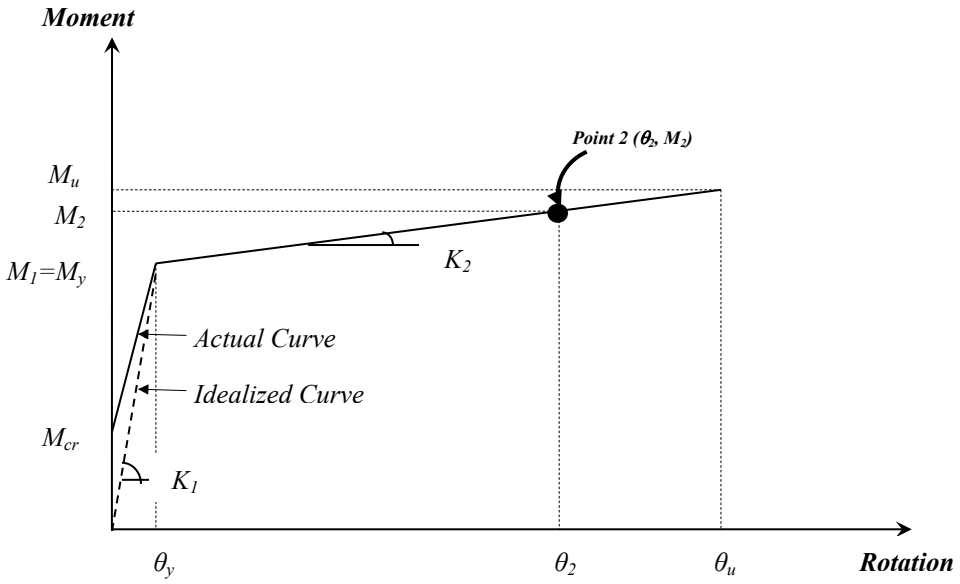


**Figure (4):** Moment-Rotation Model of Bond-Slip Spring under Monotonic Load

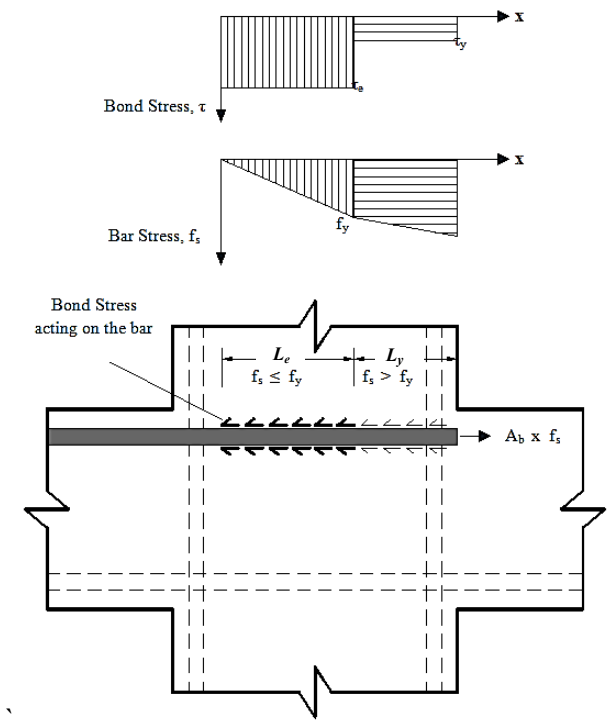


**Figure (5):** Rebar Bond-Slip under Monotonic Load

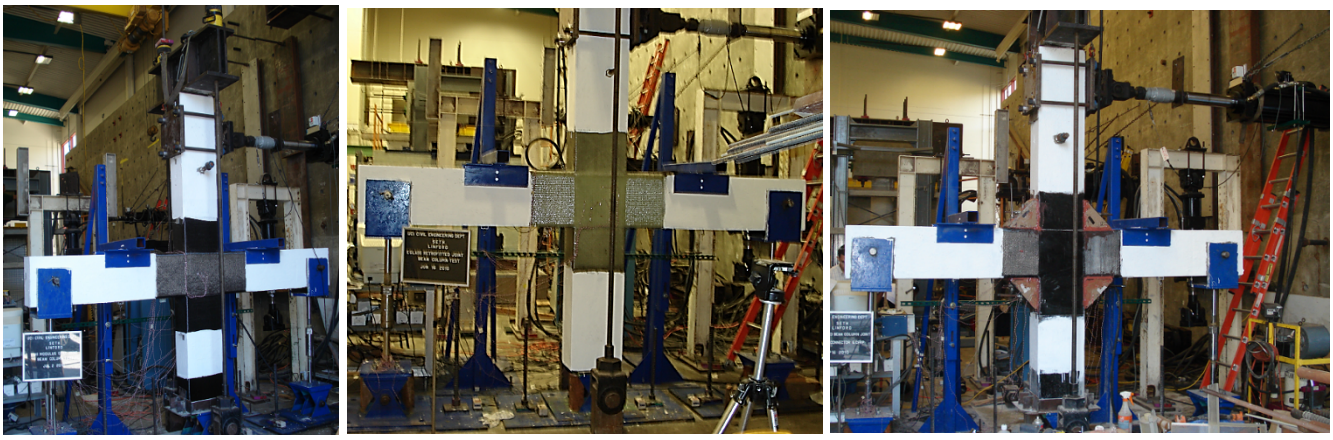

***(a)*** ***(b)*** ***(c)***

**Figure (6):** Samples of Full-Scale Beam-Column Joint Specimens Evaluated by Allam et al. (2018): *(a) Carbon/Epoxy Shear Retrofitted Specimens, (b) E-glass/Epoxy Shear Retrofitted Specimens, (c) Carbon/Epoxy Bond-slip Retrofitted Specimens*

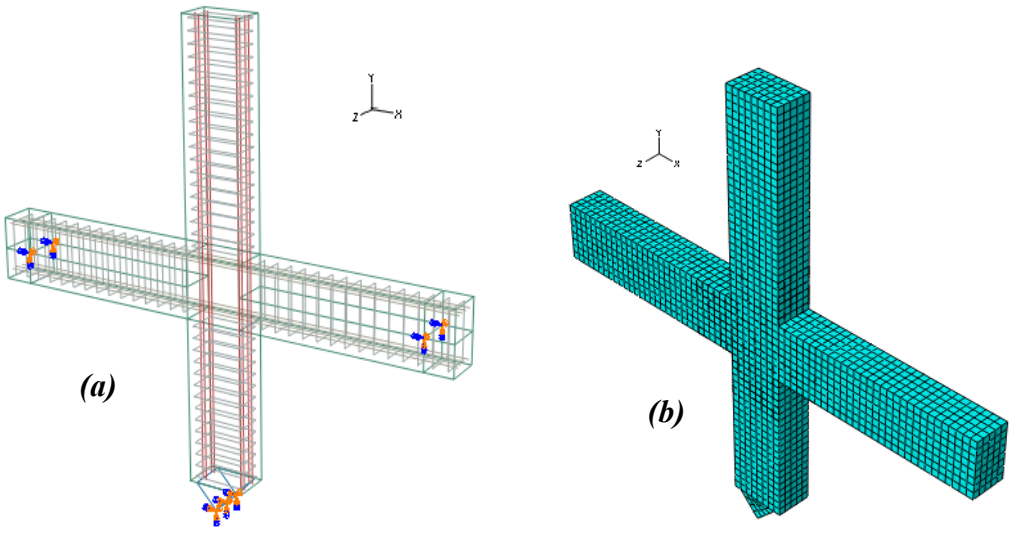


**Figure (7):** (a) Finite Element Model, (b) FE Model Mesh

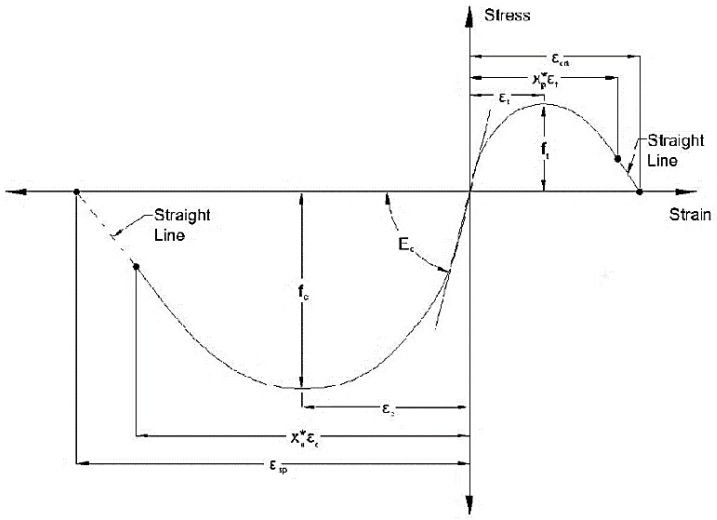


**Figure (8):** Concrete Uniaxial Compressive Stress-Strain Curve

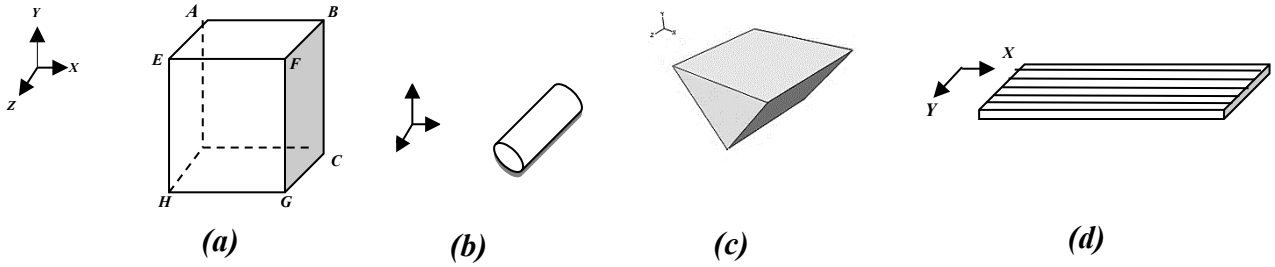


**Figure (9):** FE Elements: *(a) Concrete Solid Element (C3D8R), (b) Steel Rebar Truss Element (T3D2), (c) Steel Hinge Support Solid Element, (d) FRP Shell Element (S4R)*

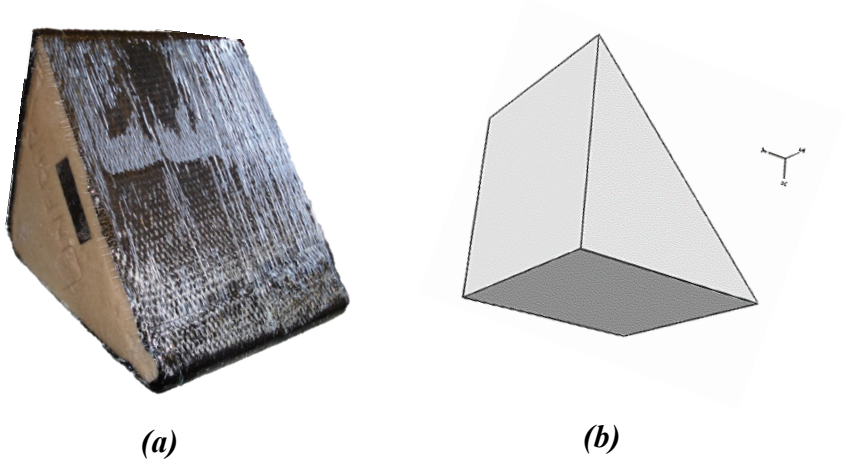


**Figure (10):** (a) The Hybrid Composite Connector (HCC), (b) Solid Element (C3D8R) Used in FE Modeling of HCC

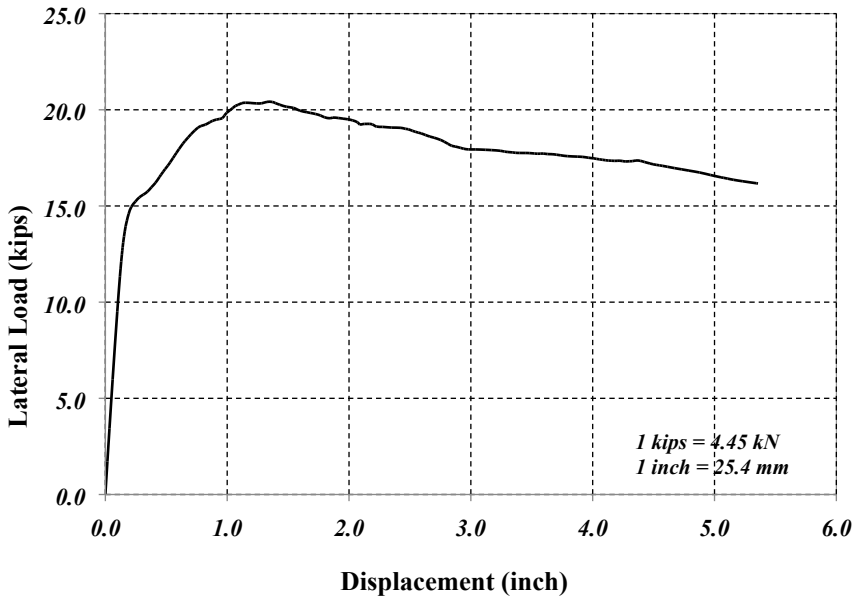


**Figure (11):** FE Model Load-Displacement Curve for Control (As-built) Specimen

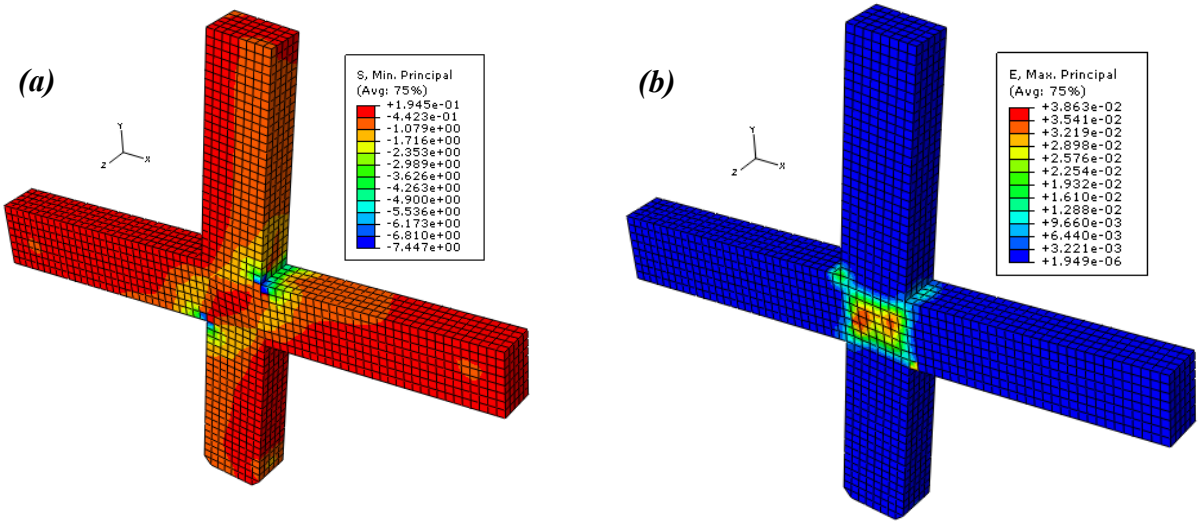


**Figure (12):** Control Specimen's Concrete Principal Stresses:

*(a) Principal Stresses, (b) Principal Strains*

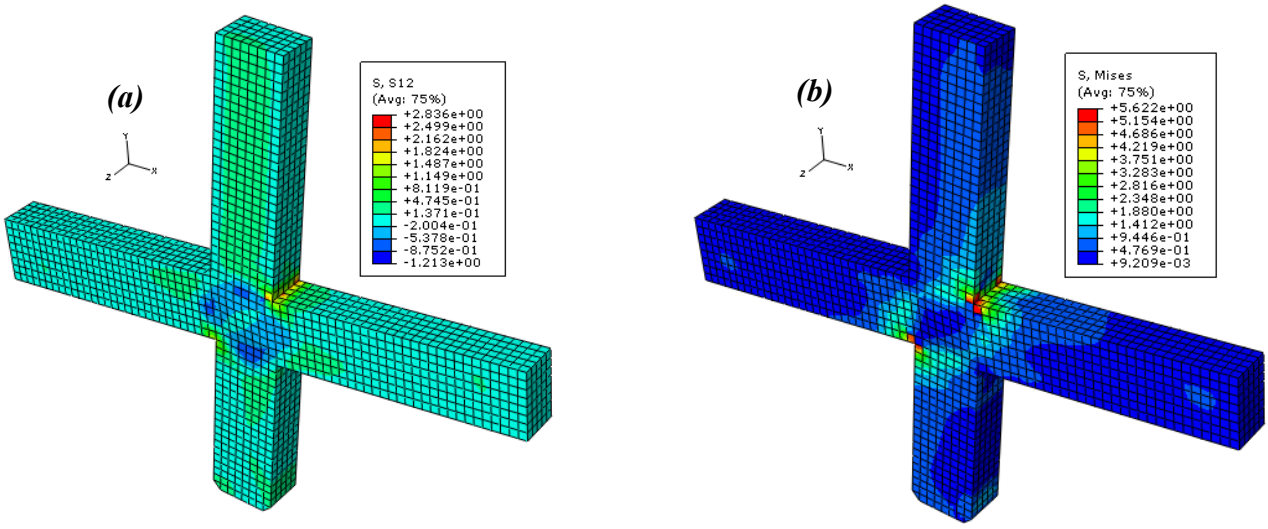


**Figure (13):** Control Joint Specimen Contours: *(a) Shear Stresses, (b) Von-Mises Stresses*

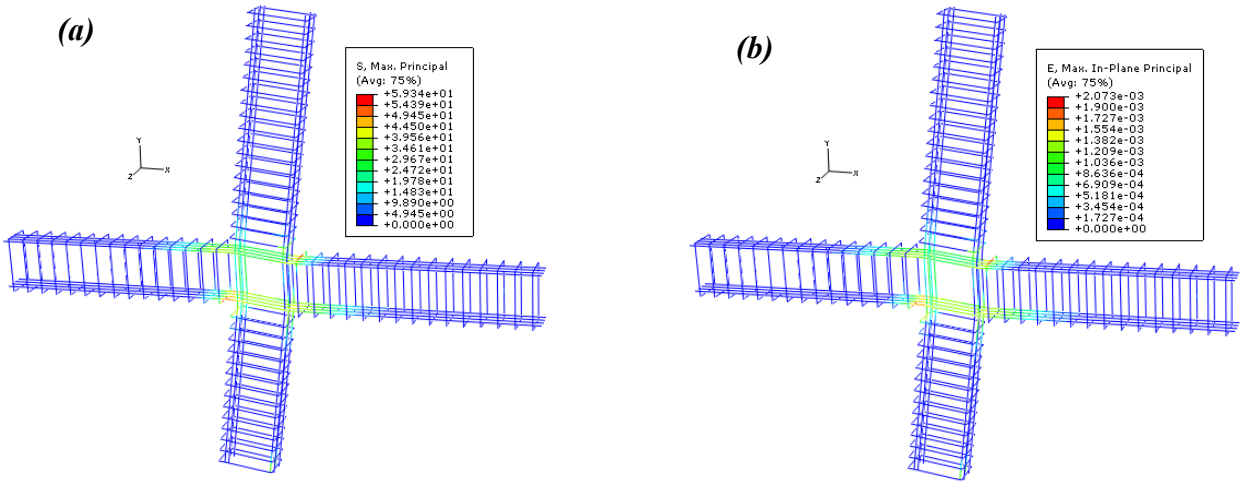


**Figure (14):** Control Specimen Steel Rebars Distribution of: *(a) Stresses, (b) Strains.*

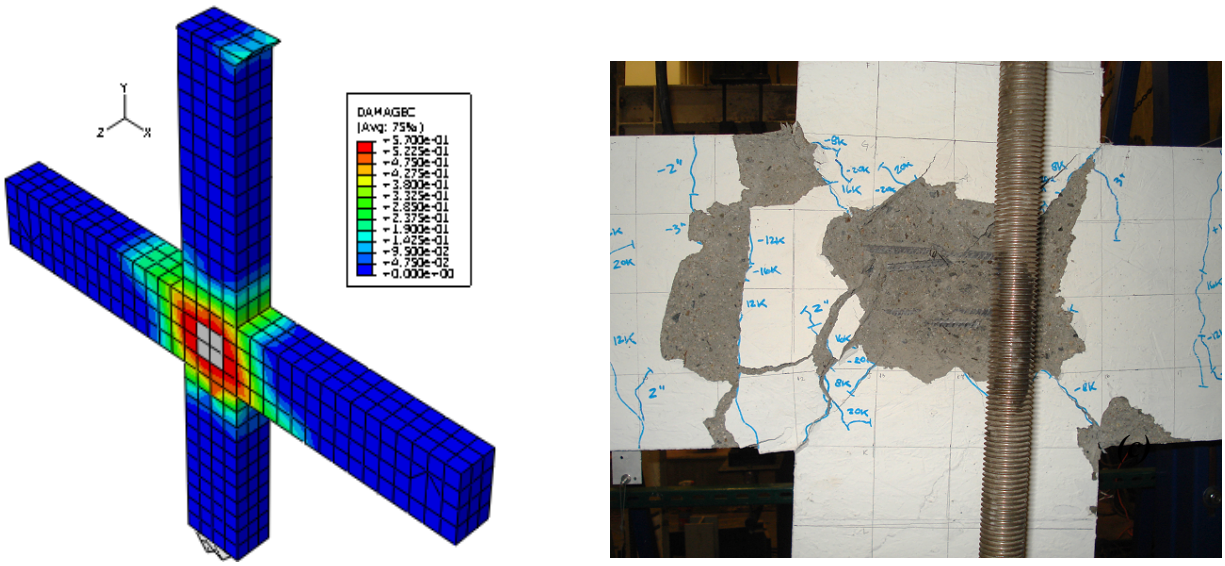


**Figure (15):** Control Specimen Failure*: (a) Simulated, (b) Experiment*

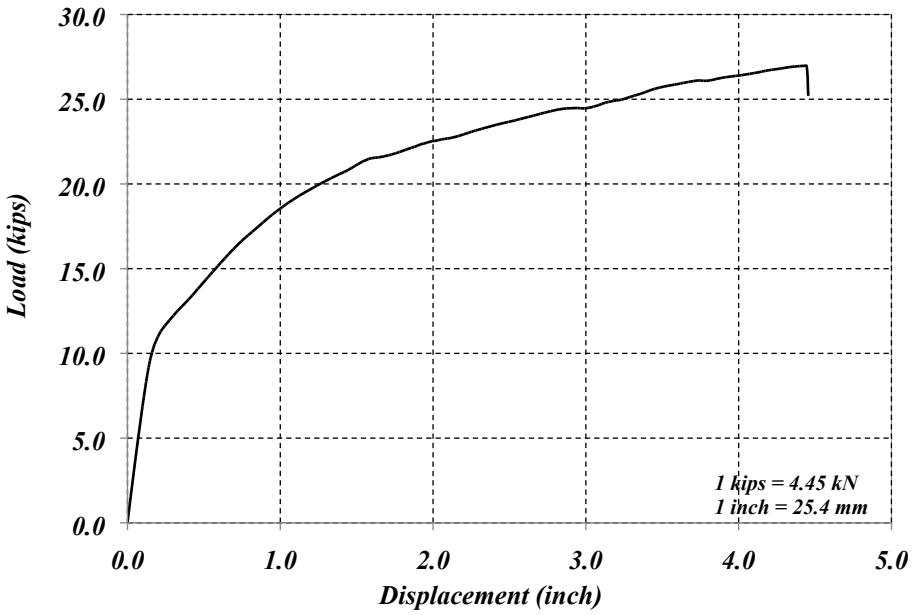


**Figure (16):** Specimen (RS-SC) Simulated Load-Displacement Curve

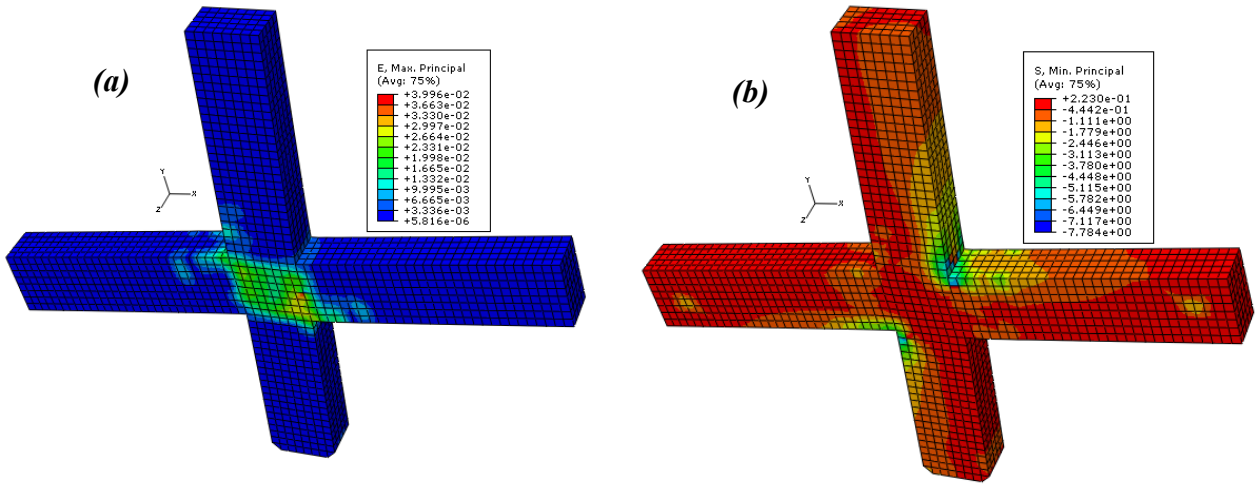


**Figure (17):** Retrofitted Specimen (RS-SC) Concrete Principal Stresses: *(a) Maximum, (b) Minimum*

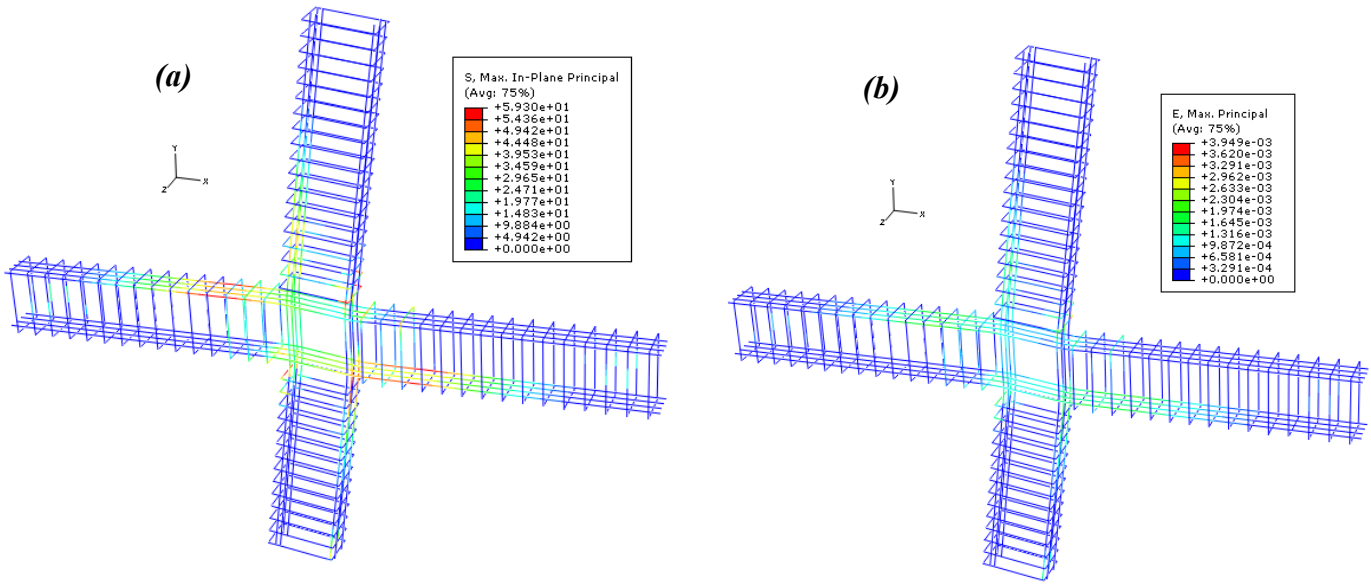


**Figure (18):** Retrofitted Specimen (RS-SC) Steel Rebars Distribution of: *(a) Stresses, (b) Strains*.

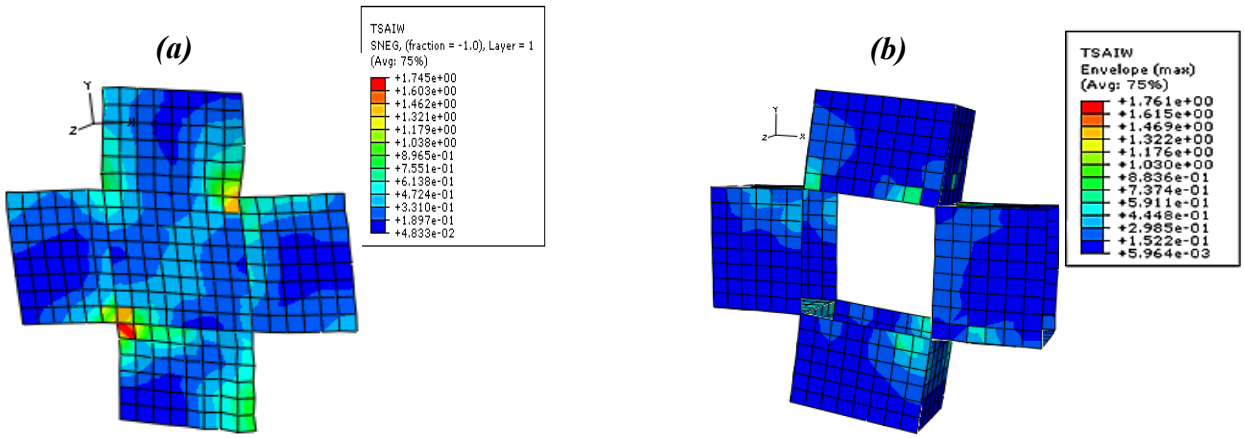


**Figure (19):** Tsai-Wu Failure Criterion for High-Strength CFRP Laminates used in Retrofitted Specimen (RS-SC): *(a) at Joint Region, (b) at Beams*

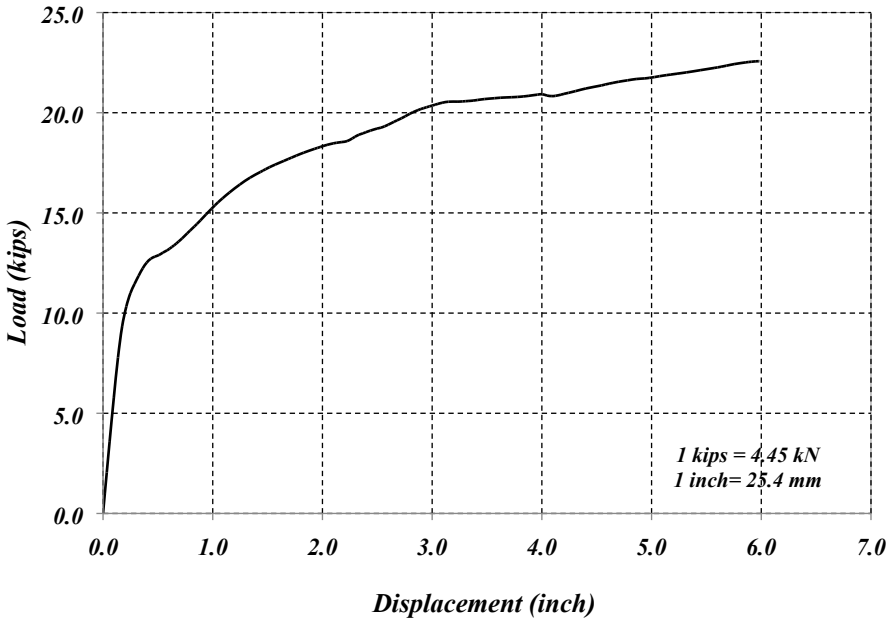


**Figure (20):** Specimen (RS-G) Simulated Load-Displacement Curve

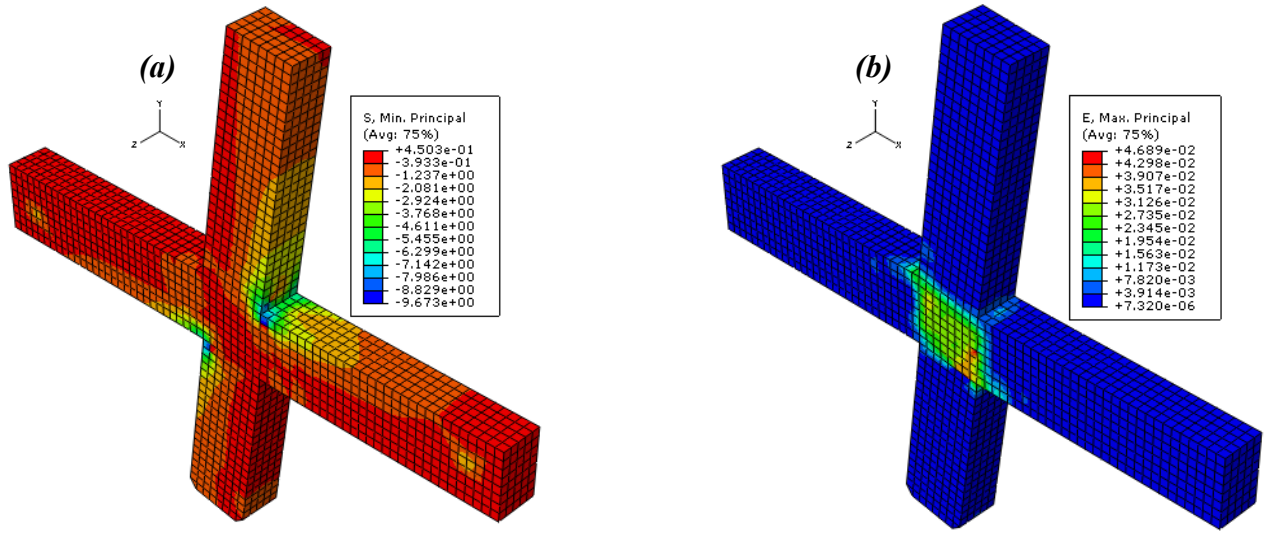


**Figure (21):** Retrofitted Specimen (RS-G) Concrete Principal Stresses: *(a) Maximum, (b) Minimum*

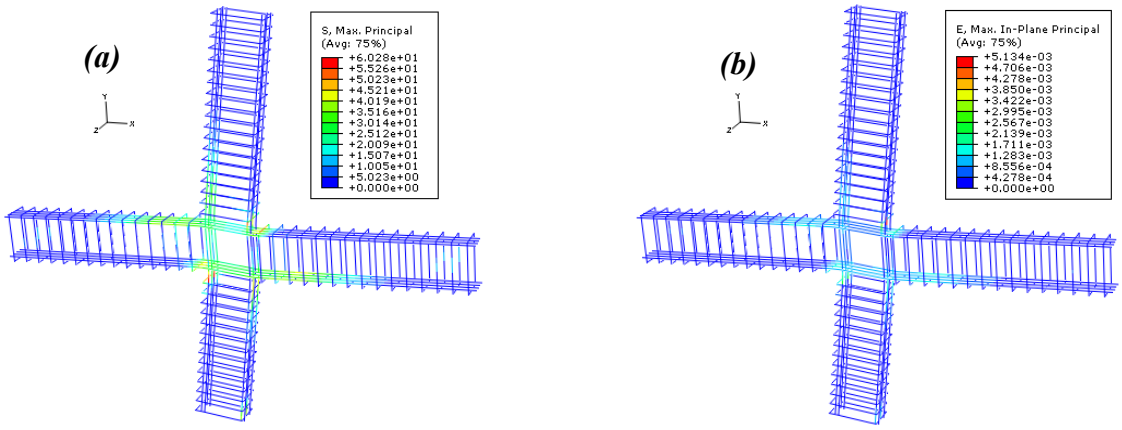


**Figure (22):** Retrofitted Specimen (RS-G) Steel Rebars Distribution of: *(a) Stresses, (b) Strains*.

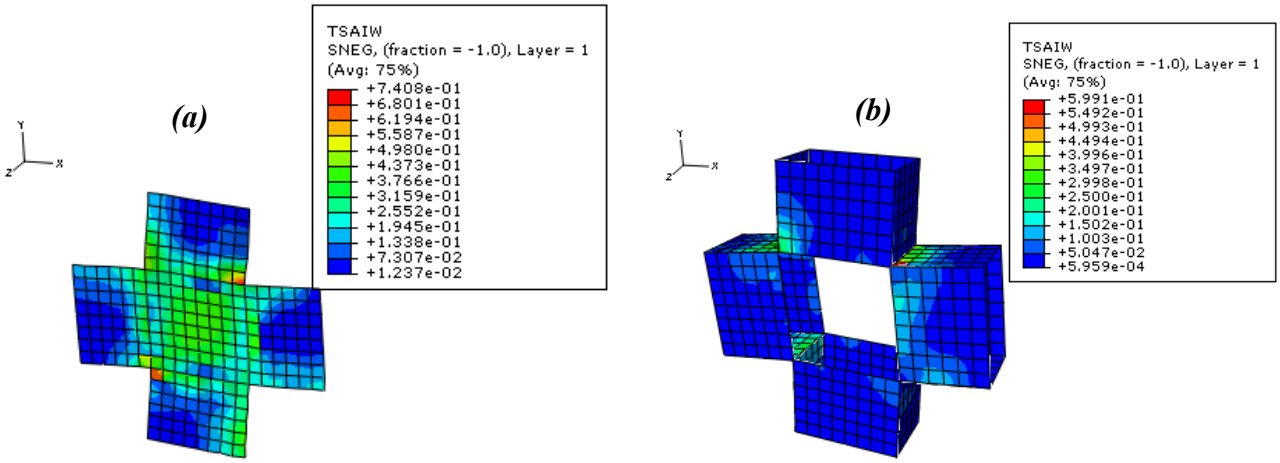


**Figure (23):** Tsai-Wu Failure Criterion for High-Strength CFRP Laminates used in Retrofitted Specimen (RS-G): *(a) at the Joint Region, (b) at the Beams and Column*

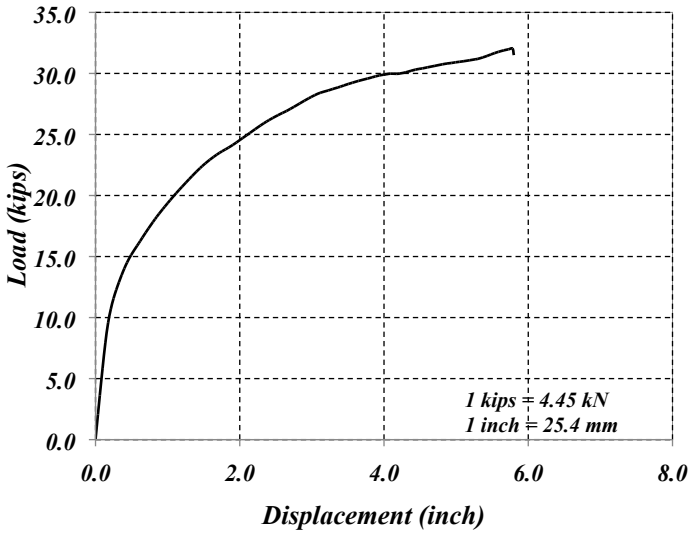


**Figure (24):** FE Model Load-Displacement Curve for Specimen (RS-MC)

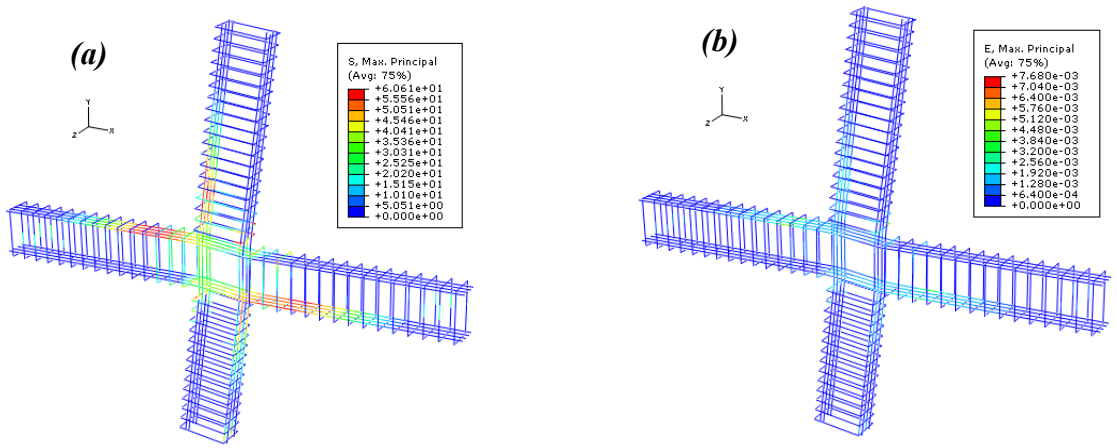


**Figure (25):** Retrofitted Specimen (RS-MC) Steel Rebars Distribution of: *(a) Stresses, (b) Strains*.

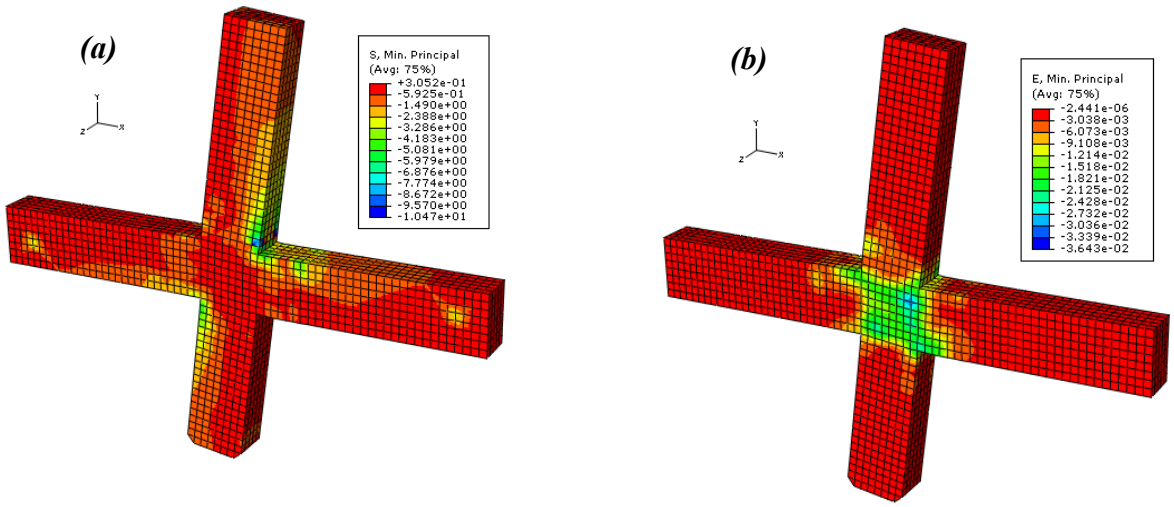


**Figure (26):** Retrofitted Specimen (RS-MC) Concrete Principal Stresses:
*(a) Principal Stresses, (b) Principal Strains*

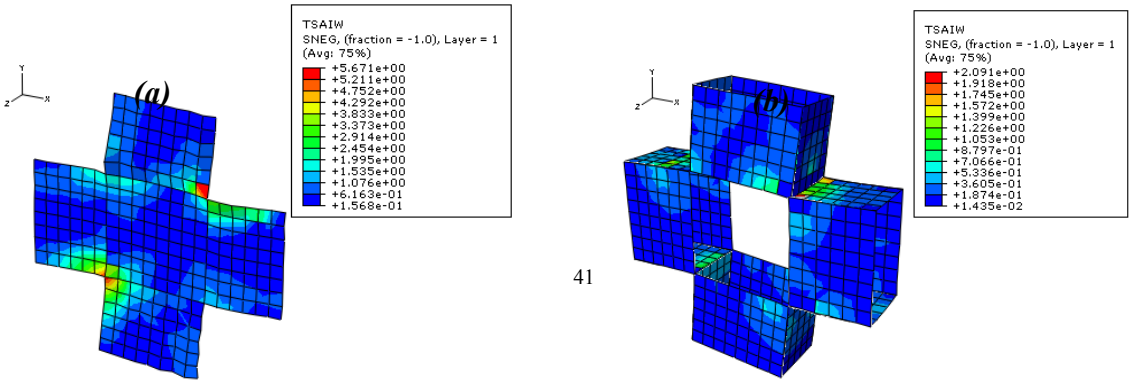

**Figure (27):** Tsai-Wu Failure Criterion for High-Strength CFRP Laminates used in Retrofitted Specimen (RS-MC): *(a) at the Joint Region, (b) at the Beams and Column*

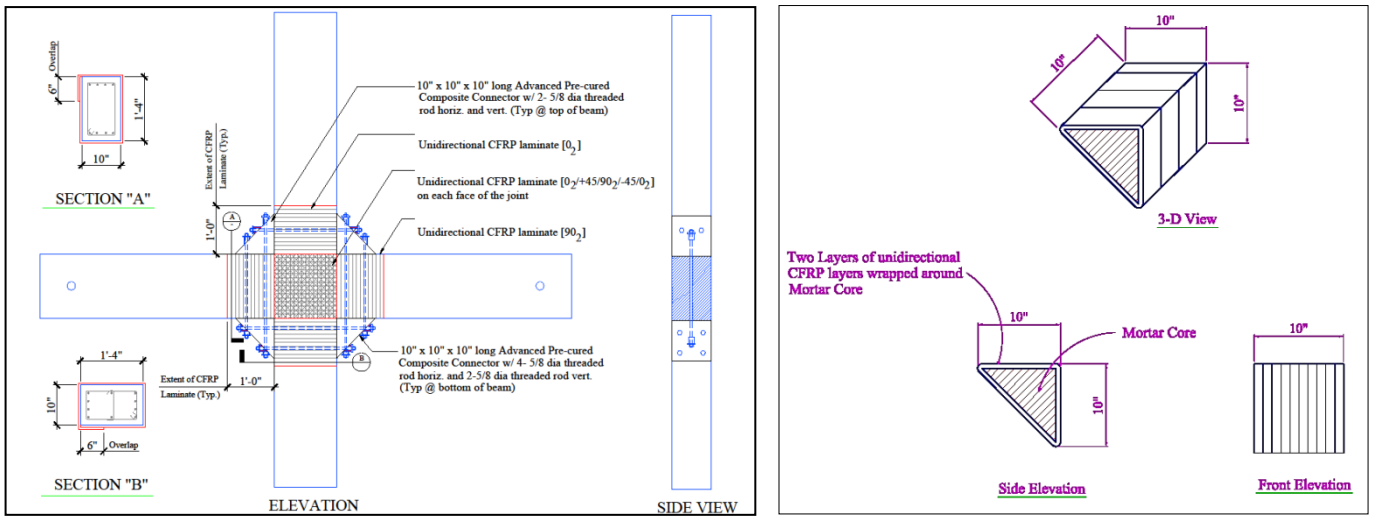


***(a)*** ***(b)***

**Figure (28):** Details of Retrofitted Specimen (RS-SCC): *(a) Combined Retrofit, (b) HCC Details*

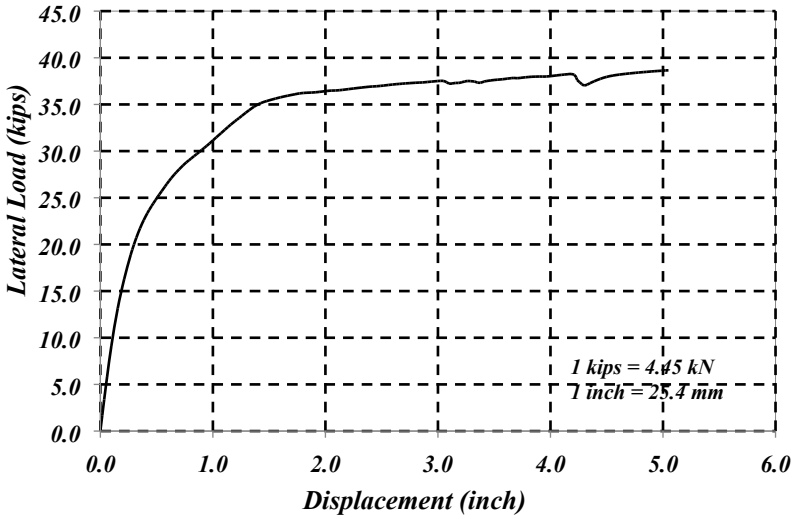

**Figure (29):** FE Model Load-Displacement Curve for Specimen (RS-SCC)

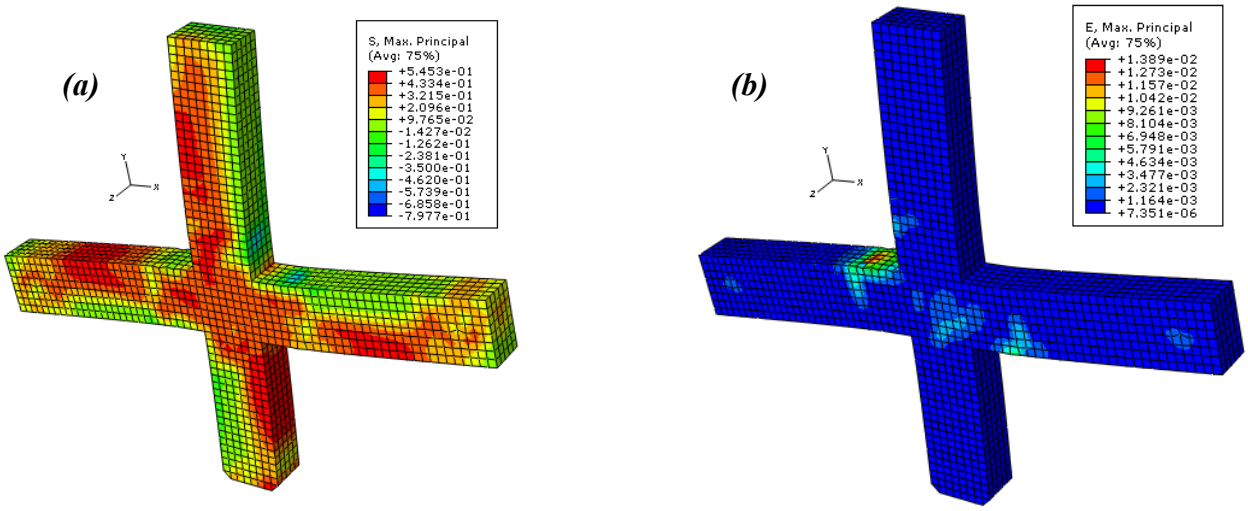


**Figure (30):** Retrofitted Specimen (RS-SCC) Concrete Principal Stresses:
*(a) Principal Stresses, (b) Principal Strains*

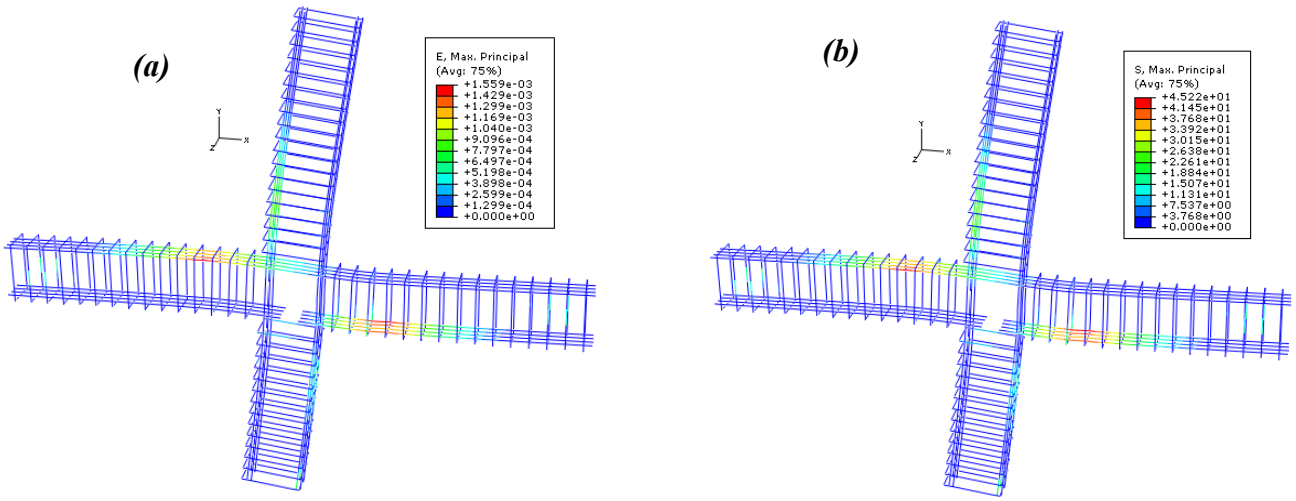

**Figure (31):** Retrofitted Specimen (RS-SCC) Steel Rebars Distribution of: *(a) Stresses, (b) Strains*.

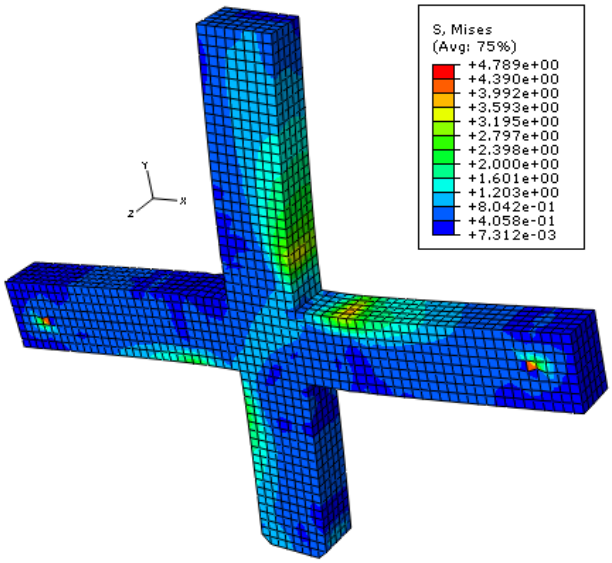


**Figure (32):** Von-Mises Stresses in Retrofitted Specimen (RS-SCC)

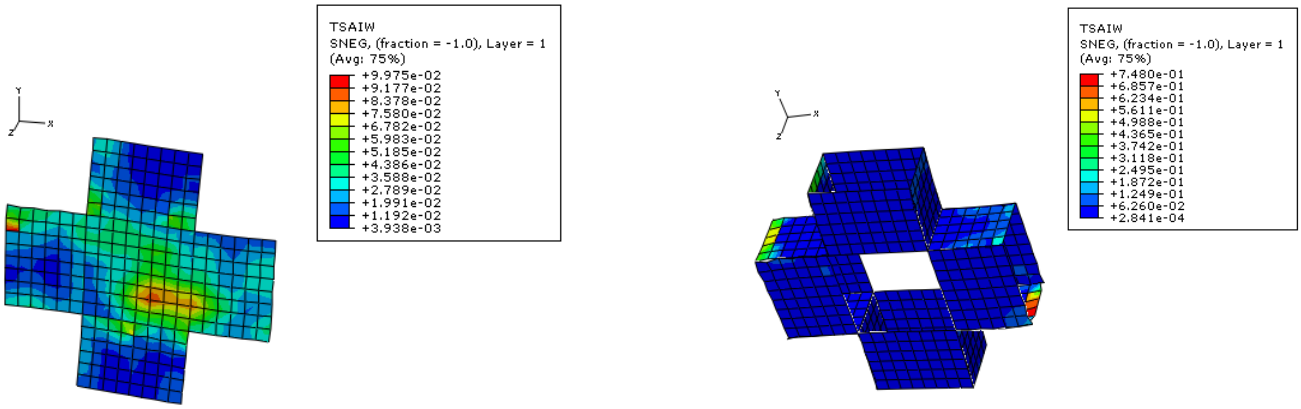


**Figure (33):** Tsai-Wu Failure Criterion for High-Strength CFRP Laminates used in Retrofitted Specimen (RS-SCC): *(a) at the Joint Region, (b) at the Beams and Column*

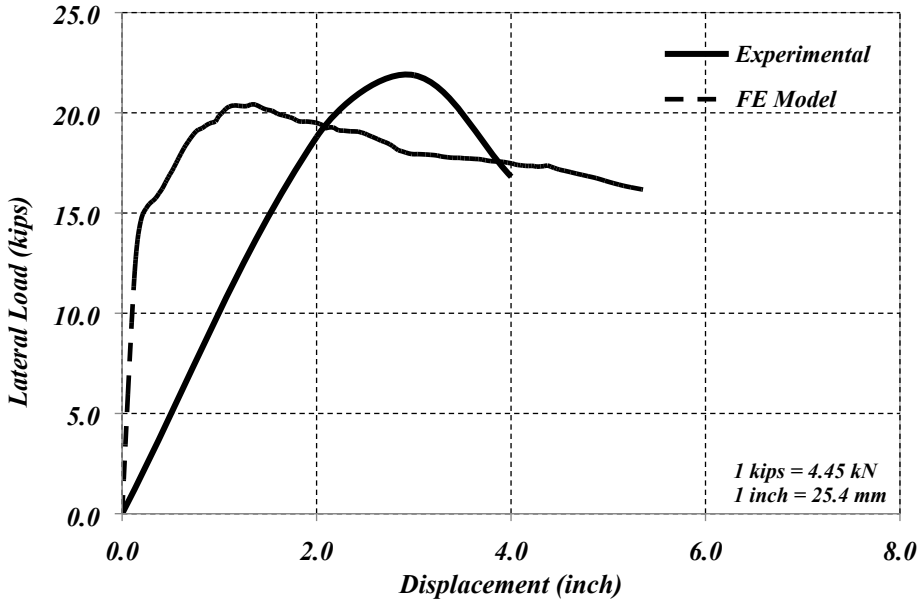


**Figure (34):** Comparison of Load-Displacement curve for Control Specimen (AB-2)

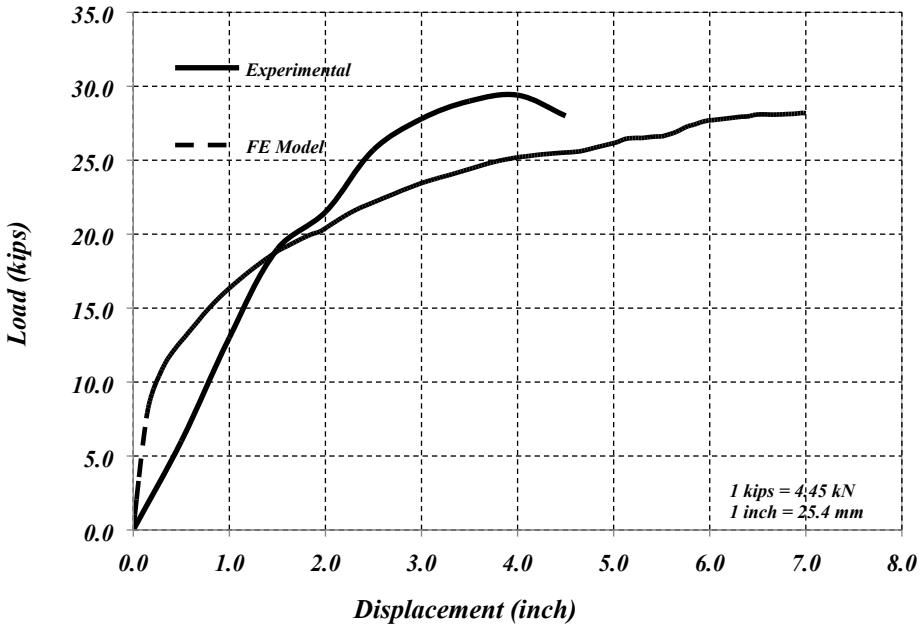


**Figure (35):** Comparison of Load-Displacement Curve for Retrofitted Specimen (RS-SC)

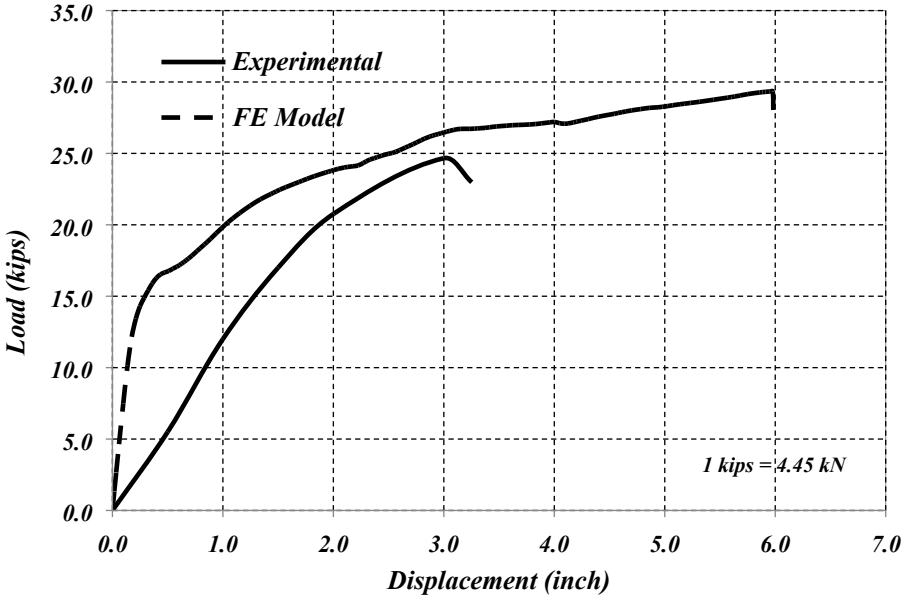


**Figure (36):** Comparison of Load-Displacement Curve for Retrofitted Specimen (RS-G)

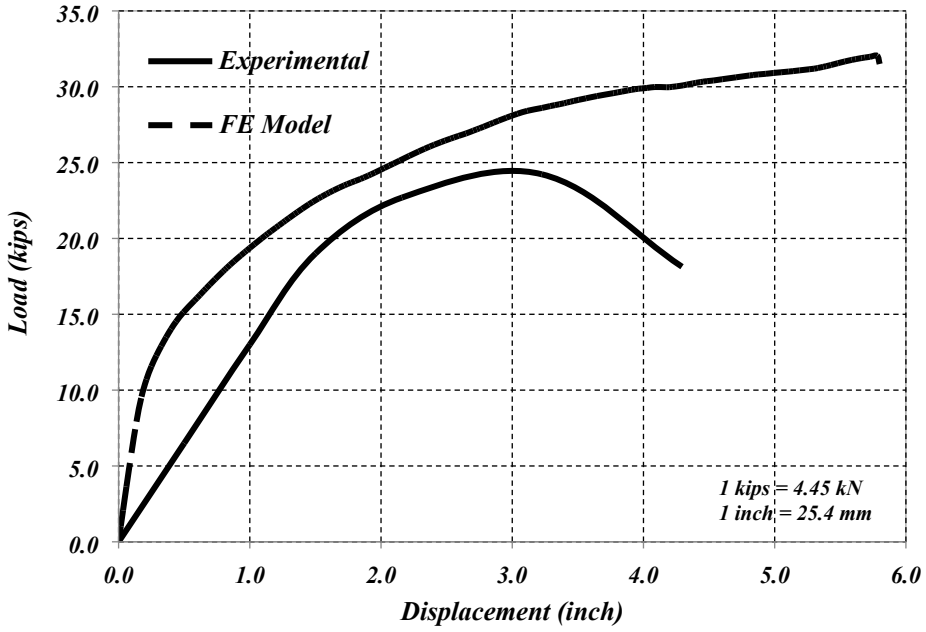


**Figure (37):** Comparison of Load-Displacement Curve for Retrofitted Specimen (RS-MC)

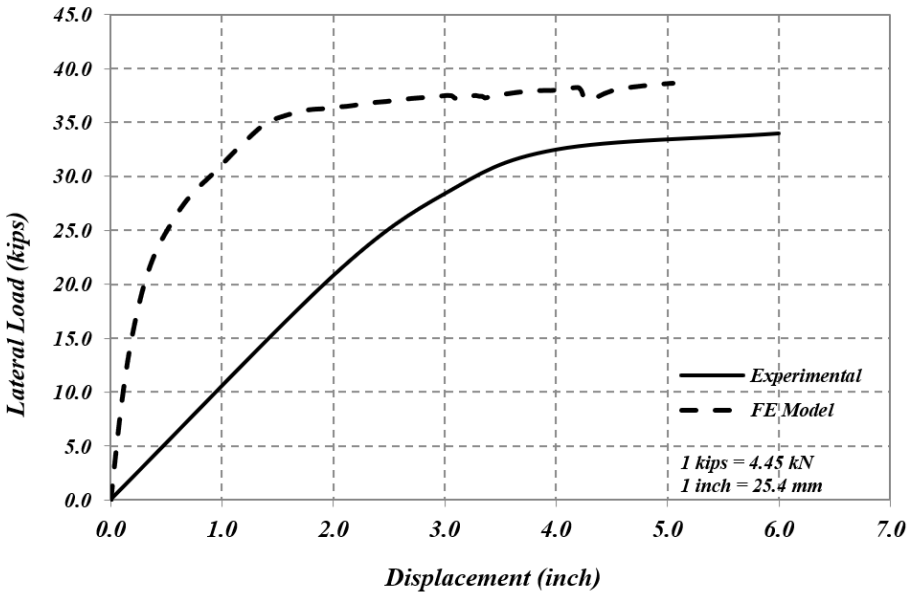


**Figure (38):** Comparison of Load-Displacement Curve for Retrofitted Specimen (RS-SCC)

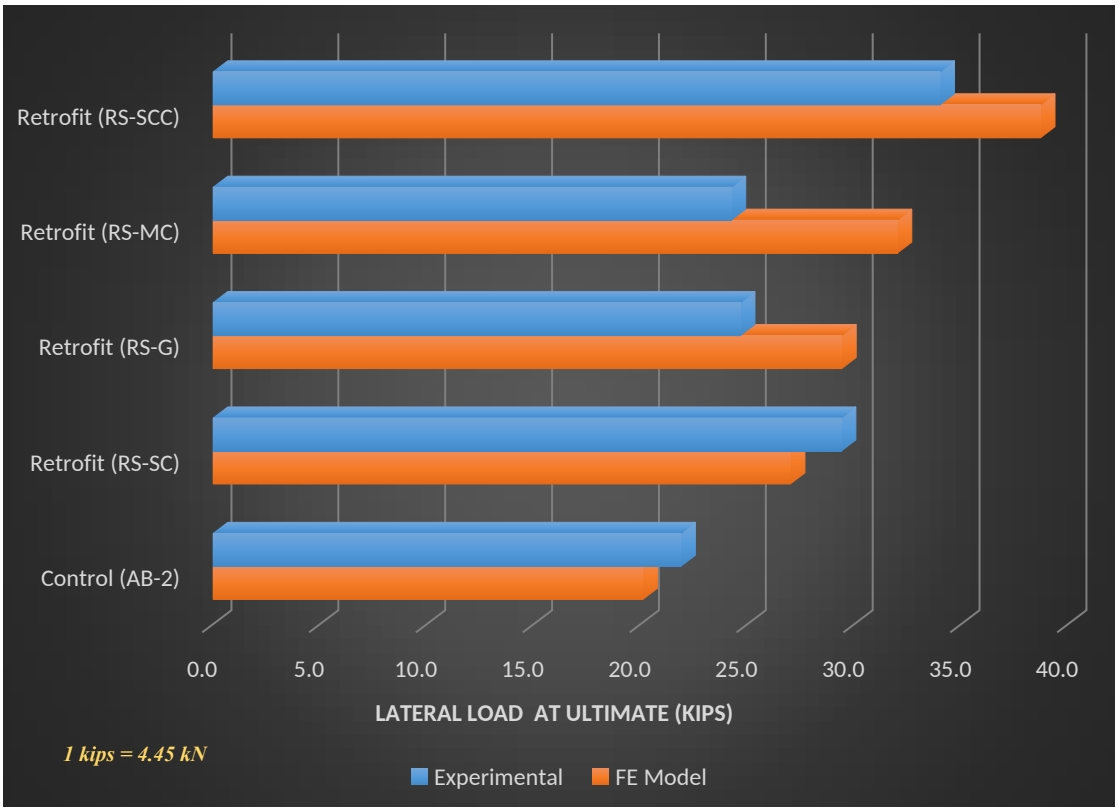


**Figure (39):** Comparison of Ultimate Load between Experimental and FE Model